Mechanical Systems and Signal Processing 232 (2025) 112704

Contents lists available at ScienceDirect

Mechanical Systems and Signal Processing

journal homepage: www.elsevier.com/locate/ymssp

Full Length Article

Enhancing bandwidth of triboelectric vibration energy harvesters through magnetic tuning

Chaoyang Zhao [a], Xin Li [b], Liwei Dong [a], Guobiao Hu [c], Chengjia Han [a], Yiqing Dong [a], Liya Zhao [d], Yaowen Yang [a,*]

[a] School of Civil and Environmental Engineering, Nanyang Technological University, 50 Nanyang Avenue, 639798, Singapore
[b] Guanzhou Institute of Technology, Xidian University, Guangzhou, Guangdong 510555, China
[c] Thrust of Internet of Things, The Hong Kong University of Science and Technology (Guangzhou), Nansha, Guangzhou 511400, China
[d] School of Mechanical and Manufacturing Engineering, University of New South Wales, Sydney 2052 NSW, Australia

ARTICLE INFO

Keywords:
Triboelectric energy harvester
Ultra-bandwidth
Vibro-impact
Electro-mechanical model
Magnetic configurations

ABSTRACT

This paper presents a novel design approach for ultra-wideband triboelectric vibration energy harvesters (UWBTVEH) by utilizing magnetic interactions to enhance performance. The triboelectric transducer operates through the coupled effect of two triboelectric layers, with nonlinear hardening and softening behaviors precisely controlled using both attractive and repulsive magnetic forces. This mechanism enables easy adjustment of beam resonances, resulting in a significantly broadened bandwidth. The approach is validated with a cost-effective UWBTVEH prototype comprising two cantilever beams, middle plates, magnet pairs and triboelectric transducers operating in a contact-separation mode. Nonlinear magnetic forces acting on the beams further influence the dynamic behavior of the triboelectric layers. Theoretical and experimental analyses demonstrate that the harvester, equipped with top and bottom magnet pairs at a 14 mm gap distance, achieves a bandwidth of 11.7 Hz under a base acceleration of 0.6 g. This performance marks a 72 % increase in the bandwidth compared to conventional triboelectric energy harvesters without magnet tuning under the same conditions. An electro-mechanical model was established and validated through experiments, demonstrating that the model effectively captures the key features of the harvester, including its wideband behavior, voltage output magnitude and asymmetric voltage signal. Furthermore, the energy generation capability of the UWBTVEH was demonstrated by powering an IoT sensing module, enabling wireless signal transmission. In summary, the proposed methodology offers valuable guidance for designing UWBTVEHs, making it particularly significant in applications involving variable-frequency energy sources.

1. Introduction

The world is advancing into a new era dominated by the Internet of Things (IoT), where the success of IoT heavily relies on the deployment of numerous electronic sensors, including temperature, humidity, GPS, and laser sensors [1–3]. These sensors are typically powered by chemical batteries, which are cumbersome and usually require regular replacement. Small-scale energy harvesting has

* Corresponding author.
E-mail address: cywyang@ntu.edu.sg (Y. Yang).

https://doi.org/10.1016/j.ymssp.2025.112704
Received 4 January 2025; Received in revised form 3 March 2025; Accepted 3 April 2025
Available online 14 April 2025

Nomenclature

E_1	Young's modulus of top beam
I_1	Moment of inertia of top beam
C_{s1}	Viscous damping coefficient of top beam
C_{a1}	Air damping coefficient of top beam
m_1	Mass per unit length of top beam
M_{t1}	Tip mass of top beam
F_c	Impact force
c_c	Impact damping coefficient
L_2	Length of bottom beam
$w_1(x,t)$	Transverse displacement of top beam
$v_1(x,t)$	Transverse velocity of top beam
d_0	Initial gap distance between
F_{mb}	Total magnetic force applied on bottom beam
V_m	Volume of the permanent magnet
d_h	Horizontal distance between two magnets
T	Distance from the centroid to the magnet surface
$\gamma_{j,r}(t)$	r^{th} modal coordinate for beam j ($j = 1,2$ represent top and bottom beams)
$I_{t,j}$	Rotary inertia of the tip mass for beam j ($j = 1,2$ represent top and bottom beams)
$\omega_{j,r}$	r^{th} modal frequency for beam j ($j = 1,2$ represent top and bottom beams)
$\zeta_{2,r}$	r^{th} modal damping ration for bottom beam
f_c	Modal impact force
f_{mb}	Modal magnetic force applied on bottom beam
R	External resistance
S	Surface area of the triboelectric material
ε_r	Relative permittivity of the triboelectric material
σ	Surface charge density of the triboelectric material
$g(t)$	Tip relative displacement between triboelectric layers
E_2	Young's modulus of bottom beam
I_2	Moment of inertia of bottom beam
C_{s2}	Viscous damping coefficient of bottom beam
C_{a2}	Air damping coefficient of bottom beam
m_2	Mass per unit length of bottom beam
M_{t2}	Tip mass of bottom beam
k_c	Impact stiffness
L_1	Length of top beam
L_c	Impact location along the beam
$w_2(x,t)$	Transverse displacement of bottom beam
$v_2(x,t)$	Transverse velocity of bottom beam
F_{ma}	Total magnetic force applied on top beam
B_r	Residual flux density of the magnet
μ_0	Permeability of vacuum
R_0	Radius of the cylindrical magnet
$\varphi_{j,r}(x)$	r^{th} Modal shape for beam j ($j = 1,2$ represent top and bottom beams)
$\lambda_{j,r}$	r^{th} eigenvalues for beam j ($j = 1,2$ represent top and bottom beams)
$\delta_{j,rs}$	Dirac function
$\zeta_{1,r}$	r^{th} modal damping ration for top beam
$f_{base,j}$	Modal excitation force for beam j ($j = 1,2$ represent top and bottom beams)
f_{ma}	Modal magnetic force applied on top beam
$z_0(t)$	Base excitation acceleration
Q	Transferred charge between two electrodes
d	Thickness of the triboelectric material
ε_0	Vacuum permittivity
ϑ	Equivalent coefficient

emerged as a promising solution for harnessing the ambient energy sources, such as vibrations, into electricity to fully replace batteries or to charge them, thereby reducing the frequency of replacements. There are various energy generation mechanisms depending on the nature of the energy source. Examples include electromagnetic harvesters [4,5], piezoelectric harvesters [6–8], photoelectric

harvesters [9,10] and thermal energy generators [11,12]. However, each of these technologies has its limitations: electromagnetic energy harvesters are heavy and bulky, piezoelectric materials are brittle, photoelectric harvesters are limited to daytime operation, and thermal transducers require a significant heat gradient. In recent years, triboelectric energy harvesters have emerged as a viable solution for harnessing vibrational energy due to their numerous advantages, such as being light-weight, flexible, cost-effective and capable of generating high power density [13–15].

Numerous triboelectric energy harvesters have been proposed for capturing vibration energy. For example, *Wu et al.* designed a harvester using spring-mass system, capable of converting energy from low-frequency vibration source [16]. *Li et al.* proposed a harvester working in a vertical sliding mode, which can generate either alternating current (AC) or direct current (DC) depending on the operation zones [17]. *Chen et al.* introduced an elastic-beam harvester consisting of an arc-stainless steel foil and an acrylic substrate. This harvester offers multiple functionalities, including acceleration, force and vibration sensing, in addition to energy harvesting [18]. Origami-inspired structures have garnered significant attention in energy harvesting due to their unique ability to form complex shapes, provide reconfigurability, and maintain flexibility. For instance, *Hu et al.* design a triboelectric energy harvester based on an origami-inspired structure, which is constructed by folding the PTFE and conductive stripes. This design tremendously increases contract aera utilization and delivers a power output of 200 μW in a manual tapping test [19]. Given that vibrations can originate from multiple directions, *He et al.* proposed a three-dimensional triboelectric-electromagnetic hybrid energy harvester. The main structure consists of a hollow sphere with a rolling ball placed inside. The ball moves and interacts with triboelectric materials attached to the inner surface of the sphere, responding to excitations from any direction [20].

It is important to note that vibration frequencies are seldom constant in real-world environment; rather, they typically vary within a certain range. Conventional triboelectric energy harvester achieves optimal power output when the source frequency aligns with their resonant frequency. However, even a slight deviation from its resonance can result in a significant decrease in output due to the harvester's narrow operational bandwidth [21,22]. This limitation highlights the need for designing wideband energy harvesters to effectively harness vibrational energy. Researchers have increasingly focused on developing design methodologies for wideband triboelectric energy harvesters, exploring approaches such as impact nonlinearity, multimodal configurations, nonlinear springs and bistable mechanisms. For harvesters working in the contact-separation mode, the induced impact between the triboelectric pairs introduces a nonlinear impact force, leading to hardening of the spring stiffness and a shift in the resonant frequency [23]. A common approach to obtain a wideband energy harvester involves utilizing this nonlinear impact force [24]. For instance, *Yang et al.* developed a wideband harvester using nonlinear elastomer beams in a miniaturized design, with a resonant frequency around 105 Hz and evident wideband behavior under a base excitation of 1.0 g [25]. *Gupta et al.* reported a wideband energy harvester using a nonlinear polymer spring [26]. *Dhakar et al.* investigated the effect of micro structured triboelectric surface on harvester bandwidth [27]. *Yang et al.* designed a 3D harvester with a circular mass block connected by three springs, capable of harnessing energy from three-dimensional directions and demonstrating a total bandwidth of 35 Hz within the range of 30 Hz to 65 Hz under an excitation acceleration of 6 m s^{-2} [28]. Some research has explored multimodal structures to achieve wideband energy harvesting. For example, *Tang et al.* investigated a two-degree-of-freedom cantilever-type harvester that has two resonant peaks and a broad bandwidth [29]. Combining multiple energy harvesting units with various resonant frequencies can effectively broaden the overall bandwidth of the system. However, this approach typically requires complex circuitry to integrate the outputs from individual units. Such deployment poses additional challenges, and optimizing the power generation performance of each unit under specific excitations remains difficult to achieve [30]. Bistable structures have been extensively studied in the design of piezoelectric energy harvesters due to their ability to achieve large-amplitude intrawell oscillations, thereby maximizing power output [31,32]. However, these bistable structures cannot be directly applied to the design of contact-separation triboelectric energy harvesters, as the impact forces may hinder intrawell oscillation. In case of sliding-mode triboelectric energy harvesters, frictional force rather than impact force is applied to the contact surface [33]. Scholars have employed bistable structures to create wideband sliding-mode energy harvester. *Tan et al.* proposed a bow-type structure comprising a slider connected to two cantilever beams via a linkage mechanism. It has a total bandwidth of 2 Hz ranging from 4.5 Hz to 6.5 Hz under a base acceleration of 3.0 g [34]. *Luo et al.* designed a bistable harvester inspired by dipteran flight, incorporating a spring, slider and linkage mechanism, resulting in a bandwidth of 4 Hz ranging from 3 Hz to 7 Hz [35]. While sliding mode harvesters offer the advantage of wide bandwidth in the extremely low-frequency range (< 10 Hz), achieving wideband characteristics typically requires interwell oscillation within the bistable structure, which usually occurs under large acceleration. Additionally, the contact-separation mode has been shown to be more efficient than the sliding mode for harnessing vibrational energy [36].

To address the challenge of developing a wideband harvester capable of operating under low-frequency and low-acceleration conditions, this study introduces a novel approach that leverages magnetic interactions. The effectiveness of this approach is demonstrated through an ultra-wide bandwidth triboelectric vibration energy harvester (UWBTVEH) prototype. The UWBTVEH utilizes a two-degree-of freedom vibrating system, incorporating lightweight and flexible cantilever beams. Operating in contact-separation mode, the harvester inherently exhibits impact nonlinearity. Nonlinear magnetic forces are integrated into the UWBTVEH design, leveraging their effectiveness in tuning structural resonance as demonstrated in other studies [37–39]. Section 2 provides a detailed description of the UWBTVEH design, followed by an introduction to the electro-mechanical modeling process in Section 3. The experimental setup for testing the UWBTVEH prototypes is introduced in Section 4. Experimental results, discussion and model validation are presented in Section 5, while Section 6 examines the power generation performance and wideband characteristics of the harvester. The study ends with a conclusion of findings and implications.

2. Methodology

The utilization of nonlinearity is one of the most widely adopted approaches in the design of wideband energy harvesters.

Triboelectric energy harvesters operating in contact-separation mode inherently exhibit impact nonlinearity due to the periodic contact and separation of the triboelectric layers. Typically, the triboelectric pair can be modeled as a two-degree-of-freedom (2DOF) system. In conventional 2DOF energy harvesters, there are two distinct resonant frequencies as indicated by the solid line in Fig. 1. This characteristic allows the system to achieve a relatively wide bandwidth, attributed to the presence of these two resonant peaks (denoted as ω_{n1} and ω_{n2}). According to the half-power bandwidth definition, the bandwidth of the conventional 2DOF harvester is denoted as $\Delta\omega_1$. To further broaden the bandwidth, the resonant peaks can be strategically shifted in opposite directions by introducing nonlinearity into the system. Specifically, the first peak (ω_{n1}) can be shifted to the left (ω'_{n1}) and the second peak (ω_{n2}) can be shifted to the right (ω'_{n2}), as illustrated by the dashed line in Fig. 1. This modification leads to a significantly expanded bandwidth, referred to as $\Delta\omega_2$. However, controlling impact nonlinearity is inherently challenging as it depends on several difficult-to-define parameters, including impact stiffness and damping. Besides, impact only results in hardening of the contacting layer and does not facilitate bidirectional frequency tuning. To achieve a further broadened bandwidth, it becomes necessary to introduce external nonlinearity into the system. Electricity is generated as long as the two layers make contact and the objective of wideband design is to ensure consistent contact between the layers over a broad range of excitation frequencies. Magnetic configurations have proven to be an effective method for introducing displacement-dependent nonlinear restoring force into vibratory systems. For a typical clamped-free cantilever beam with a magnetic configuration applied at its free end, the restoring force (f_r) in such the system can be expressed as follows:

$$f_r = (k_a + k_b)w + k_c w^3. \tag{1}$$

Here, $k_a + k_b$ represents the liner term of the spring force, while k_c denotes the cubic nonlinear component. w corresponds to the deflection of the beam. The system exhibits different nonlinear behaviors depending on the values of these parameters. For $k_a + k_b > 0$, the system shows hardening nonlinear behavior when $k_c > 0$, meaning that the stiffness of the system increases with displacement, leading to higher resonant frequencies. Conversely, when $k_c < 0$, the system demonstrates softening behavior, where the stiffness decreases with displacement, resulting in lower resonant frequencies. In the case where $k_a + k_b < 0$, the potential energy of the system develops two stable equilibrium points, which induces bistability in the system. The term k_a represents the linear stiffness of the structure itself. Terms k_b and k_c and are associated with the magnetic interactions, which cannot be adjusted independently. For instance, altering the distance between the two magnets affects both k_b and k_c and simultaneously. Therefore, by strategically employing magnetic configurations for the triboelectric layers, bidirectional resonance tuning of the system can be achieved, thereby realizing a further broadened bandwidth. This design methodology is validated through the development of a proposed harvester. The detailed structural design of the harvester is given in the following section.

3. Structural design

Cantilever beams are used as the host structure to construct the energy harvester considering its inherent design flexibility. Magnets pairs are strategically placed near the right end of each beam to introduce the desired nonlinear effect as shown in below Fig. 2. The top magnet pair is in a repulsive configuration, while the bottom magnet pair is in an attractive configuration. Taking the top magnet pair as an example, the magnets are embedded inside acrylic blocks. The block connected to the cantilever beam also functions as the tip mass, which can be adjusted to tune the natural frequency of the beam. Another block is mounted on a vertical support that can move in the horizontal direction to adjust the gap between two magnets, thereby finetuning the system's nonlinearity. The triboelectric pair is formed on fiberglass-reinforced epoxy plates (FR4) positioned between the two cantilever beams. The left end of the plate is connected to a spacer, while the right end is linked to the beam via a support. Elastomers are used in these connections to avoid any rigid contact that could negatively affect the dynamic behavior of the harvester. The spacer and support also control the gap distance between the two plates. It is worthwhile to mention that the natural frequency of top beam (ω_{n1}) is intentionally designed to be lower than that of the bottom beam (ω_{n2}). This design choice is critical for achieving the desired wide bandwidth. In this case, the repulsive magnetic force acting on the top beam causes a softening effect, shifting ω_{n1} to the left (towards lower frequencies). The attractive magnetic force on the bottom beam leads to the hardening effect, shifting ω_{n2} to the right (towards higher frequencies). The vibration of the beams makes the middle plates contact and separate with each other periodically. The detailed electricity generation mechanism of this UWBTVEH will be discussed in the following section.

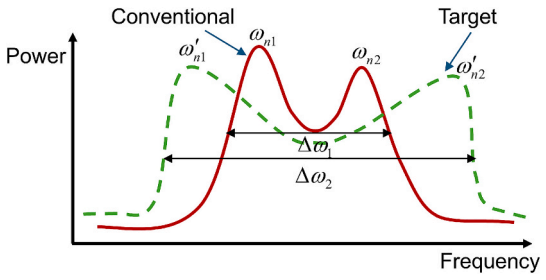

Fig. 1. Bandwidth broadening mechanism of triboelectric energy harvesters.

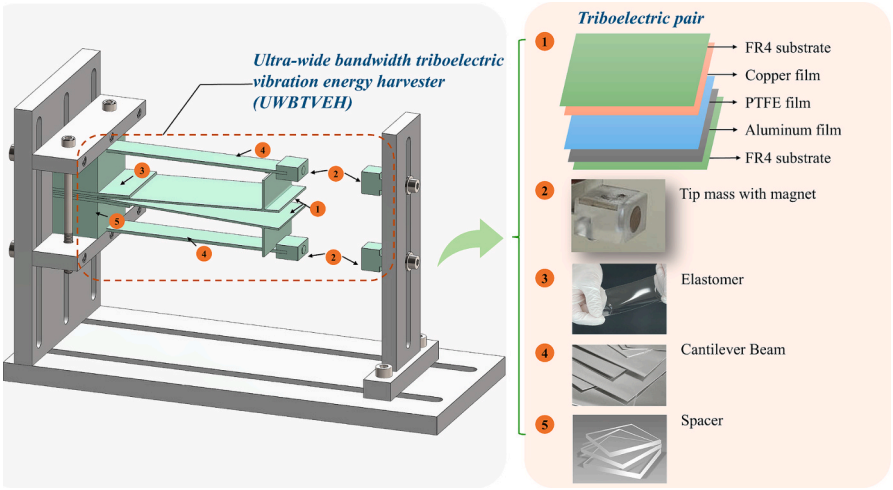

Fig. 2. Structural diagram of the developed ultra-wide bandwidth triboelectric vibration energy harvester.

The electricity generation of UWBTVEH is based on the triboelectrification and electrostatic induction within the triboelectric pair. As shown in Fig. 3, the triboelectric pair comprises a copper electrode, an aluminum electrode and a PTFE (polytetrafluoroethylene) film, with the PTFE film bonded to the aluminum electrode. In the initial state, the PTFE film and copper electrode are in compact contact, and no charge transfer occurs between two electrodes. However, due to triboelectrification, negative charges are generated on the surface of PTFE film, while an equal amount of positive charge is induced on the surface of the copper electrode because of the electrostatic induction. As the system begins to operate, the copper electrode starts to separate from the PTFE film, forming an angle θ. At this moment, the negative charge begins to transfer from the aluminum electrode to the copper electrode through an external circuit due to the high voltage potential difference created by the PTFE film. This charge transfer continues and reaches its maximum when the separation angle θ reaches its maximum value θ_{max}. Subsequently, as the copper electrode and PTFE film move closer to each other, eventually realizing full contact, the negative charge flows from the copper electrode to the aluminum electrode. This cyclical process of contact and separation causes the negative charges to flow back and forth through the external circuit, thereby generating an alternating current.

4. Modeling of UWBTVEH

4.1. Mechanical model

To formulate the electro-mechanical model of the UWBTVEH, the harvester is simplified as a two-beam structure. The middle plates are treated as additional mass applied to the beams, given the absence of a rigid connection between the beams and middle plates. Thus, the dynamic behavior of the UWBTVEH primarily depends on the host beams. The simplified model is shown in Fig. 4. The governing equations are established based on the Euler-Bernoulli beam theory as follows [40,41].

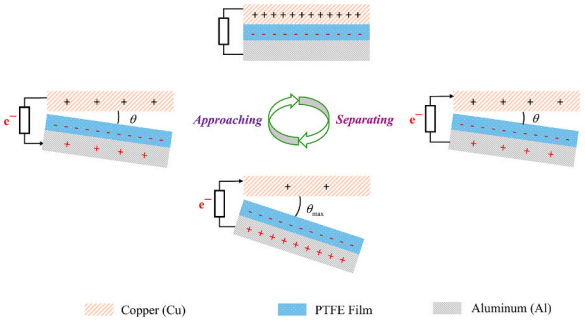

Fig. 3. Electricity generation mechanism of triboelectric pair.

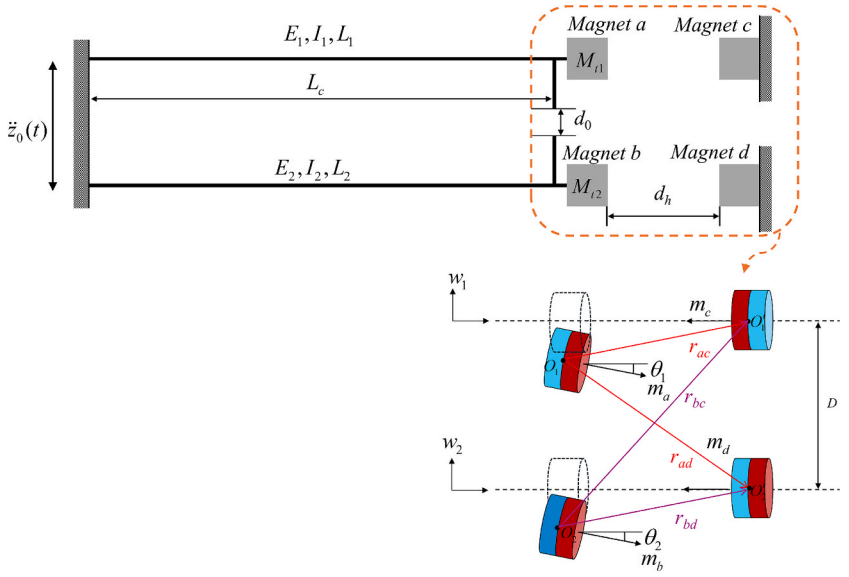

Fig. 4. Simplified structural diagram of the UWBTVEH for model construction.

$$\begin{cases} \dfrac{\partial^2}{\partial x^2}\left[E_1 I_1 \dfrac{\partial^2 w_1(x,t)}{\partial x^2}\right] + c_{s1} I_1 \dfrac{\partial^5 w_1(x,t)}{\partial x^4 \partial t} + c_{a1}\dfrac{\partial w_1(x,t)}{\partial t} + m_1 \dfrac{\partial^2 w_1(x,t)}{\partial t^2} \\ \quad = -[m_1 + M_{t1}\delta(x-L_1)]\dfrac{d^2 z_0(t)}{dt^2} + F_c\delta(x-L_c) + F_{ma}\delta(x-L_1) \\ \dfrac{\partial^2}{\partial x^2}\left[E_2 I_2 \dfrac{\partial^2 w_2(x,t)}{\partial x^2}\right] + c_{s2} I_2 \dfrac{\partial^5 w_2(x,t)}{\partial x^4 \partial t} + c_{a2}\dfrac{\partial w_2(x,t)}{\partial t} + m_2 \dfrac{\partial^2 w_2(x,t)}{\partial t^2} \\ \quad = -[m_2 + M_{t2}\delta(x-L_2)]\dfrac{d^2 z_0(t)}{dt^2} + F_c\delta(x-L_c) + F_{mb}\delta(x-L_2). \end{cases} \tag{2}$$

In Eq. (2), subscripts 1 and 2 represent the top and bottom cantilever beams, respectively. Here, E_1 and E_2 are the Young's moduli, while I_1 and I_2 denote the moments of inertia for each of the two beams. The terms C_{s1}, C_{s2}, C_{a1} and C_{a2} represent the viscous and air damping coefficients for each beam, respectively. The parameters m_1 and m_2 denote the mass per unit length of two beams, whereas M_{t1} and M_{t2} indicate the tip masses. The impact force, F_c, is represented as follows:

$$F_c = \begin{cases} 0, w_2(L_c,t) - w_1(L_c,t) - d_0 \leqslant 0 \\ k_c[w_2(L_c,t) - w_1(L_c,t) - d_0] + c_c[v_2(L_c,t) - v_1(L_c,t)], w_2(L_c,t) - w_1(L_c,t) - d_0 > 0, \end{cases} \tag{3}$$

where, k_c and c_c represent the impact stiffness and damping coefficient, respectively. The initial gap distance between the two beams is denoted by d_0, and L_c indicates the impact location on the beam. The variables w_1 and w_2 represent the vibration displacements the top and bottom beams, respectively. According to Eq. (2), no impact force is considered when the relative motion between the beams is less than the initial gap distance. The force is only included when the relative displacement exceeds this gap. The beams are also subjected to either attractive or repulsive magnetic forces due to the magnet configurations. There are three major methods to calculate the magnetic forces: (1) the magnetic dipole method (MDM) [42], (2) the equivalent magnetizing current method (EMCM) [43], and (3) the magnetic charge method (MCM) [44]. The MDM assumes that each magnet acts as a magnetic dipole located at its geometric center. This method not only provides accurate predictions of magnetic forces but also has a relatively simple form compared to the other two methods, making it particularly suitable for the electro-mechanical modeling of energy harvesters. In the UWBTVEH, two pairs of magnets are configured such that magnet *a* experiences a repulsive force from magnet *c* and an attractive force from magnet *d*. Therefore, the total force acting on magnet *a* is the combined effect of the repulsive and attractive forces exerted by magnets *c* and *d*, respectively. Similarly, the total force on magnet *b* results from the sum of the repulsive and attractive forces applied by magnets *c* and *d*. The MDM is utilized to derive the magnetic force, and the potential energy (U_{mi}) between magnets is obtained as follows:

$$U_{mi} = \frac{\kappa}{(d_h + T)^3} \cdot \frac{\alpha_i(2 - \beta_i^2 \eta_i^2)}{(1 + \beta_i^2 \eta_i^2)^{5/2}}, (i = 1, 2, 3, 4), \tag{4}$$

in which, $\kappa = {B_r}^2 {V_m}^2 / 4\pi\mu_0$. Here, μ_0 denotes the permeability of vacuum and B_r represents the residual flux density of each magnet. V_m refers to the volume of the permanent magnets. The detailed derivation can be referred to the work from *Yang et al* [45]. The

expressions of α_i, β_i and η_i are given below:

$$\begin{cases} \alpha_i = 1 - 3\mu + \dfrac{135}{64}\mu^2 + \dfrac{3}{2}\mu\eta_i^2 \\ \beta_i = 1 - 2\mu + \dfrac{321}{64}\mu^2 + \dfrac{1233}{64}\mu^3 + \dfrac{9}{4}\mu\eta_i^2 \\ \mu = R_0^2 - \dfrac{4}{3}T^2 \\ \eta_i = \{\eta_1, \eta_2, \eta_3, \eta_4\} = \left\{\dfrac{w_1}{d_h}, \dfrac{\overline{w}_1}{d_h}, \dfrac{w_2}{d_h}, \dfrac{\overline{w}_2}{d_h}\right\}, \end{cases} \tag{5}$$

where, the subscript i indicates the magnet pairs ac, ad, bc and bd. Here, w_1 and w_2 also refer to the vertical displacement of magnets a and b. $\overline{w}_1$ and $\overline{w}_2$ are related to the coordinate transformation from w_1 and w_2. In specific, $\overline{w}_1 = w_1 + D$ and $\overline{w}_2 = w_2 + D$. The parameter d_h denotes the horizontal distance between magnet a (or b) and c (or d). It is worthwhile to note that the above Eq. (5) is derived by neglecting the angles (θ_1 and θ_2) for magnets a and b considering the small vibration amplitude. The expression is also a Taylor expression that is used to avoid complex integration. The magnetic force (F_m) is derived by differentiating Eq. (4) with respect to the displacement of magnets:

$$F_m = \{F_{ma-}, F_{ma+}, F_{mb-}, F_{mb+}\} = \left\{ -\frac{\partial U_{m1}}{\partial w_1}, \frac{\partial U_{m2}}{\partial \overline{w}_1}, -\frac{\partial U_{m3}}{\partial \overline{w}_2}, \frac{\partial U_{m4}}{\partial w_2} \right\}, \tag{6}$$

here, the + and − signs indicate attractive and repulsive magnetic forces acting on each magnet. The total magnetic forces of magnets a (F_{ma}) and b (F_{mb}) can be obtained as follows:

$$\begin{cases} F_{ma} = F_{ma-} + F_{ma+} = \dfrac{3\kappa}{d^4} \cdot \left(\dfrac{\alpha_1\beta_1^2\eta_1(4 - \beta_1^2\eta_1^2)}{(1 + \beta_1^2\eta_1^2)^{7/2}} - \dfrac{\alpha_2\beta_2^2\eta_2(4 - \beta_2^2\eta_2^2)}{(1 + \beta_2^2\eta_2^2)^{7/2}} \right) \\ F_{mb} = F_{mb-} + F_{mb+} = \dfrac{3\kappa}{d^4} \cdot \left(\dfrac{\alpha_4\beta_4^2\eta_4(4 - \beta_4^2\eta_4^2)}{(1 + \beta_4^2\eta_4^2)^{7/2}} - \dfrac{\alpha_3\beta_3^2\eta_3(4 - \beta_3^2\eta_3^2)}{(1 + \beta_3^2\eta_3^2)^{7/2}} \right). \end{cases} \tag{7}$$

Eq.(2) represents a set of partial differential equations (PDEs) that can be solved using the method of separation of variables. Assuming that the displacement solution takes the form:

$$w_j(x, t) = \varphi_{j,r}(x)\gamma_{j,r}(t), \tag{8}$$

where $\varphi_{j,r}(x)$ and $\gamma_{j,r}(t)$ are the r^{th} modal shape and modal coordinate of the beams, respectively, where $j = 1,2$ represents top and bottom beams. To determine the natural frequencies and modal shapes of the beam, Eq. (2) is simplified by ignoring the damping force terms, resulting in the following form:

$$E_jI_j\frac{\partial^4 w_j(x, t)}{\partial x^4} + m_j\frac{\partial^2 w_j(x, t)}{\partial t^2} = 0, \tag{9}$$

given that the harvester is clamped at one end while the other end with a tip mass is freely hanging, the boundary conditions for the clamped-free beam components are as follows:

$$\begin{cases} w_j(0, t) = 0 \\ E_jI_j\dfrac{\partial w_j(x, t)}{\partial x}\bigg|_{x=0} = 0 \\ E_jI_j\dfrac{\partial^2 w_j(x, t)}{\partial x^2}\bigg|_{x=L} = 0 \\ E_jI_j\dfrac{\partial w_j^3(x, t)}{\partial x^3}\bigg|_{x=L} = 0, \end{cases} \tag{10}$$

substituting Eq.(8) into Eq.(9) and applying the boundary conditions specified in Eq.(10), the eigen-function for the r^{th} mode for beam j can be derived as:

$$\varphi_{j,r} = C_{j,r}\left[\cosh\frac{\lambda_{j,r}}{L}x - \cos\frac{\lambda_{j,r}}{L}x - \sigma_{j,r}\left(\sin\frac{\lambda_{j,r}}{L}x - \sinh\frac{\lambda_{j,r}}{L}x\right)\right], \tag{11}$$

where

$$\sigma_{j,r}=\frac{m_jL\left(\sin\lambda_{j,r}-\sinh\lambda_{j,r}\right)+\lambda_{j,r}M_{t,j}\left(\cos\lambda_{j,r}-\cosh\lambda_{j,r}\right)}{m_jL\left(\cos\lambda_{j,r}+\cosh\lambda_{j,r}\right)-\lambda_{j,r}M_{t,j}\left(\sin\lambda_{j,r}-\sinh\lambda_{j,r}\right)}. \tag{12}$$

The eigenvalues ($\lambda_{j,r}$) are the roots of the following characteristic equation, which accounts for the rotary inertia of the tip mass ($I_{t,j}$):

$$\begin{aligned}&1+\cos\lambda_{j,r}\cosh\lambda_{j,r}+\frac{\lambda_{j,r}M_{t,j}}{m_jL}\left(\cos\lambda_{j,r}\sinh\lambda_{j,r}-\sin\lambda_{j,r}\cosh\lambda_{j,r}\right)\\&-\frac{\lambda_{j,r}^3I_{t,j}}{m_jL^3}\left(\cosh\lambda_{j,r}\sin\lambda_{j,r}+\sinh\lambda_{j,r}\cos\lambda_{j,r}\right)+\frac{\lambda_{j,r}^4M_{t,j}I_{t,j}}{m_j^2L^4}\left(1-\cos\lambda_{j,r}\cosh\lambda_{j,r}\right)=0.\end{aligned} \tag{13}$$

The modal coefficient $C_{j,r}$ for the r^{th} mode can be determined by applying the following orthogonality conditions:

$$\begin{cases}\displaystyle\int_0^L\varphi_{j,s}(x)m_j\varphi_{j,r}(x)dx+\varphi_{j,s}(L)M_{t,j}\varphi_{j,r}(L)+\left[\frac{d\varphi_{j,s}(x)}{dx}I_{t,j}\frac{d\varphi_{j,r}(x)}{dx}\right]_{x=L}=\delta_{j,rs}\\\displaystyle\int_0^L\varphi_{j,s}(x)E_jI_j\frac{d^4\varphi_{j,r}(x)}{dx^4}dx-\left[\varphi_{j,s}(x)E_jI_j\frac{d^3\varphi_{j,r}(x)}{dx^3}\right]_{x=L}+\left[\frac{d\varphi_{j,s}(x)}{dx}E_jI_j\frac{d^2\varphi_{j,r}(x)}{dx^2}\right]_{x=L}=\omega_{j,nr}^2\delta_{j,rs},\end{cases} \tag{14}$$

where $\delta_{j,rs}$ is the Dirac function that has the below form:

$$\delta_{j,rs}\begin{cases}0, r\neq s\\1, r=s,\end{cases} \tag{15}$$

the modal frequency $\omega_{j,nr}$ can be represented as:

$$\omega_{j,nr}=\lambda_{j,r}^2\sqrt{\frac{E_jI_j}{m_jL^4}}, \tag{16}$$

subsequently, the governing equation of the system can be reformulated in terms of the modal coordinates as:

$$\begin{cases}\dfrac{d^2\gamma_{1,r}(t)}{dt^2}+2\zeta_{1,r}\omega_{1,r}\dfrac{d\gamma_{1,r}(t)}{dt}+\omega_{1,r}^2\lambda_{1,r}(t)=f_{base,1}+f_c+f_{ma}\\\dfrac{d^2\gamma_{2,r}(t)}{dt^2}+2\zeta_{2,r}\omega_{2,r}\dfrac{d\gamma_{2,r}(t)}{dt}+\omega_{2,r}^2\lambda_{1,r}(t)=f_{base,2}-f_c+f_{mb},\end{cases} \tag{17}$$

in which, the modal excitation force ($f_{base,j}$) is:

$$f_{base,j}=-\left[\int_0^L\varphi_{j,r}(x)m_jdx+\varphi_{j,r}(L)M_{t,j}\right]\frac{d^2z_0(t)}{dt^2}, \tag{18}$$

and the modal impact force (f_c) is:

$$f_c=\begin{cases}0, w_2(L_c,t)-w_1(L_c,t)-d_0\leqslant 0\\\varphi_{j,r}(L_c)k_c[w_2(L_c,t)-w_1(L_c,t)-d_0]+\\\varphi_{j,r}(L_c)c_c[v_2(L_c,t)-v_1(L_c,t)], w_2(L_c,t)-w_1(L_c,t)-d_0>0,\end{cases} \tag{19}$$

and the modal magnetic forces (f_{ma} and f_{mb}) are:

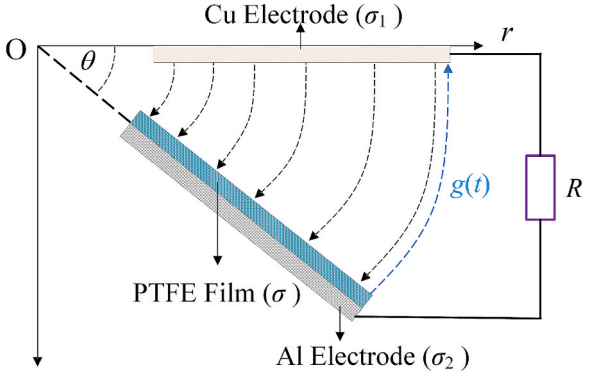

Fig. 5. Schematic of tribo-pair with non-parallel configuration.

$$\begin{cases} f_{ma} = \varphi_{j,r}(L_1)\dfrac{3\kappa}{d^4}\cdot\left(\dfrac{\alpha_1\beta_1^2\eta_1(4-\beta_1^2\eta_1^2)}{(1+\beta_1^2\eta_1^2)^{7/2}} - \dfrac{\alpha_2\beta_2^2\eta_2(4-\beta_2^2\eta_2^2)}{(1+\beta_2^2\eta_2^2)^{7/2}}\right) \\ f_{mb} = \varphi_{j,r}(L_2)\dfrac{3\kappa}{d^4}\cdot\left(\dfrac{\alpha_4\beta_4^2\eta_4(4-\beta_4^2\eta_4^2)}{(1+\beta_4^2\eta_4^2)^{7/2}} - \dfrac{\alpha_3\beta_3^2\eta_3(4-\beta_3^2\eta_3^2)}{(1+\beta_3^2\eta_3^2)^{7/2}}\right). \end{cases} \tag{20}$$

4.2. Electrical model

The electrical model of the harvester can be constructed based on the *V-Q-x* relationships, where V is the voltage, Q is the charge, and x is the displacement. Notably, the triboelectric pair in the harvester features a non-parallel configuration as shown in Fig. 5. According to our previous study, the model considering the non-parallel configuration can be formulated as follows [46,47]:

$$R\frac{dQ}{dt} + \frac{Q}{S\varepsilon_0}\left(\frac{d}{\varepsilon_r} + \vartheta g(t)\right) - \frac{\sigma\vartheta g(t)}{\varepsilon_0} = 0, Q(t=0) = 0. \tag{21}$$

where, R represents the resistance of the external load, and Q denotes the charge transferred between two electrodes. S and d are the surface area and thickness of the triboelectric material, respectively. ε_0 and ε_r are the vacuum permittivity and relative permittivity of the triboelectric material. σ is the surface charge density of the material, and ϑ represents an equivalent coefficient related to the geometrical dimensions of the tribo-pair. $g(t)$ refers to the relative displacement between triboelectric layer, $g(t) = w_2(t) - w_1(t) - d_0$.

5. Experimental setup

The UWBTVEH prototype was fabricated for a series of test using a shaker as shown in below Fig. 6. The UWBTVEH was mounted on a fixture placed on the shaker platform. A computer controlled a data acquisition (DAQ) module to record the voltage output from the UWBTVEH. The desired vibration signal was generated by the computer through a vibration controller, amplified by a power amplifier, and then transmitted to the shaker. To ensure accurate vibration acceleration measurement, an accelerometer was affixed to the top platform of the shaker. The accelerometer's readings were fed back to the controller, enabling precise regulation of the vibration acceleration. To thoroughly evaluate the performance of the UWBTVEH with its magnetic configurations, three different magnet setups were tested: (1) magnet pairs applied only to the top beam, (2) magnet pairs applied only to the bottom beam, and (3) magnet pairs applied to both the top and bottom beams. The gap distance between the triboelectric pair was found to affect the power output and bandwidth of the harvester in our previous study [48]. In general, a narrower gap attributes to higher power output and a wider bandwidth. However, a gap that is too narrow, such as 1 mm, is not recommended, as it may cause the two layers to adhere due to attractive electrostatic forces and potential manufacturing imperfections. This adhesion would increase the overall stiffness of the system, making it difficult to excite under low excitation levels. Our previous study identified 2 mm as the optimal gap distance. Furthermore, to isolate the effects of magnetic force and accurately assess its influence, the gap distance was consistently maintained at 2 mm throughout all tests. The tests were conducted by sweeping the frequency range from 6 Hz to 26 Hz and varying the acceleration between 0.3 g and 0.6 g.

Fig. 6. Experimental setup for UWBTVEH under base excitations using the shaker.

6. Results and discussion

6.1. UWBTVEH with only top magnet

Fig. 7 shows the actual configuration of UWBTVEH with a magnet pair for the top cantilever beam. In this configuration, the single

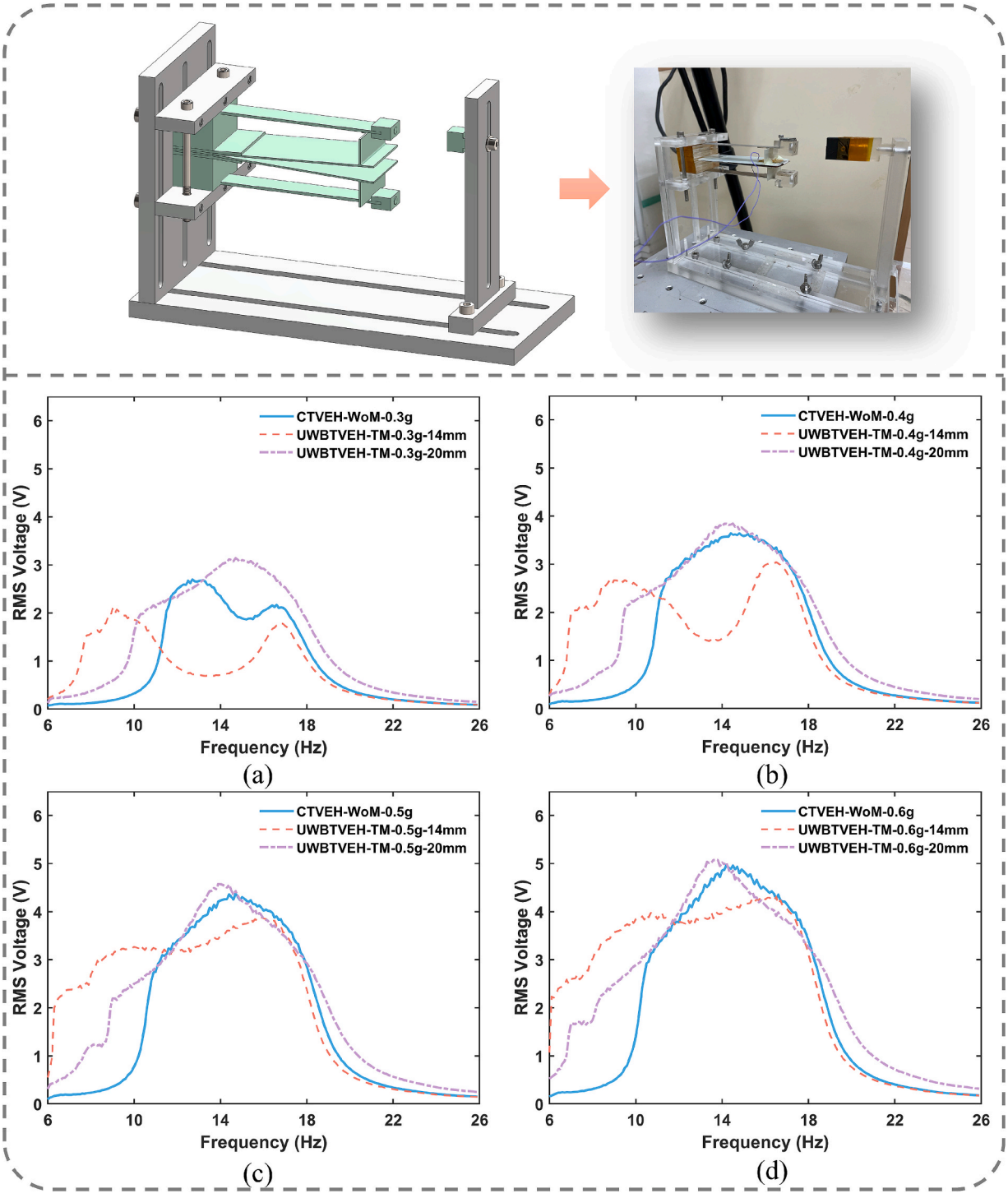

Fig. 7. UWBTVEH with only top magnet pair and RMS voltage output of UWBTVEH equipped with only top magnet pair with various gap distances and base accelerations: (a) 0.3 g; (b) 0.4 g; (c) 0.5 g and (d) 0.6 g.

magnet connected to the beam without magnet pair only serves as tip mass. For comparison, a conventional triboelectric energy harvester (CTVEH) without magnet pair was also tested. To facilitate discussion, notations CTVEH-X-Y and UWBTVEH-X-Y-Z are defined here. X denotes the magnet pair configurations (WoM: without magnet pair; TM: top magnet pair; BM: bottom magnet pair; TBM: top&bottom magnet pairs). Y refers to the excitation acceleration applied to the harvester. Z indicates the gap distances within the magnet pair. For example, UWBTVEH-TM-0.3 g-14 mm represents the UWBTVEH with a top magnet pair that has a gap distance of 14 mm, operating under a base excitation of 0.3 g. In the case of the CTVEH under low excitation, such as CTVEH-WoM-0.3 g, two distinct peaks are observed (Fig. 7(a)). The first peak occurs at the frequency of 12.8 Hz and the second peak appears at the frequency of 16.6 Hz. They are corresponding to the first natural frequencies of top and bottom beams, respectively. As the excitation increases, these two peaks merge due to frequency locking caused by the strong coupling between the beams (Fig. 7(b), (c) and (d)) [48]. This merging leads to a continuous bandwidth and higher power output, with the merged frequency occurring around 14.3 Hz, and the root mean square voltage (V_{RMS}) reaching up to 5 V for CTVEH-WoM-0.6 g as shown in Fig. 7(d).

When the top magnet pair in a repulsive configuration is introduced, a noticeable shift occurs in the first peak towards lower

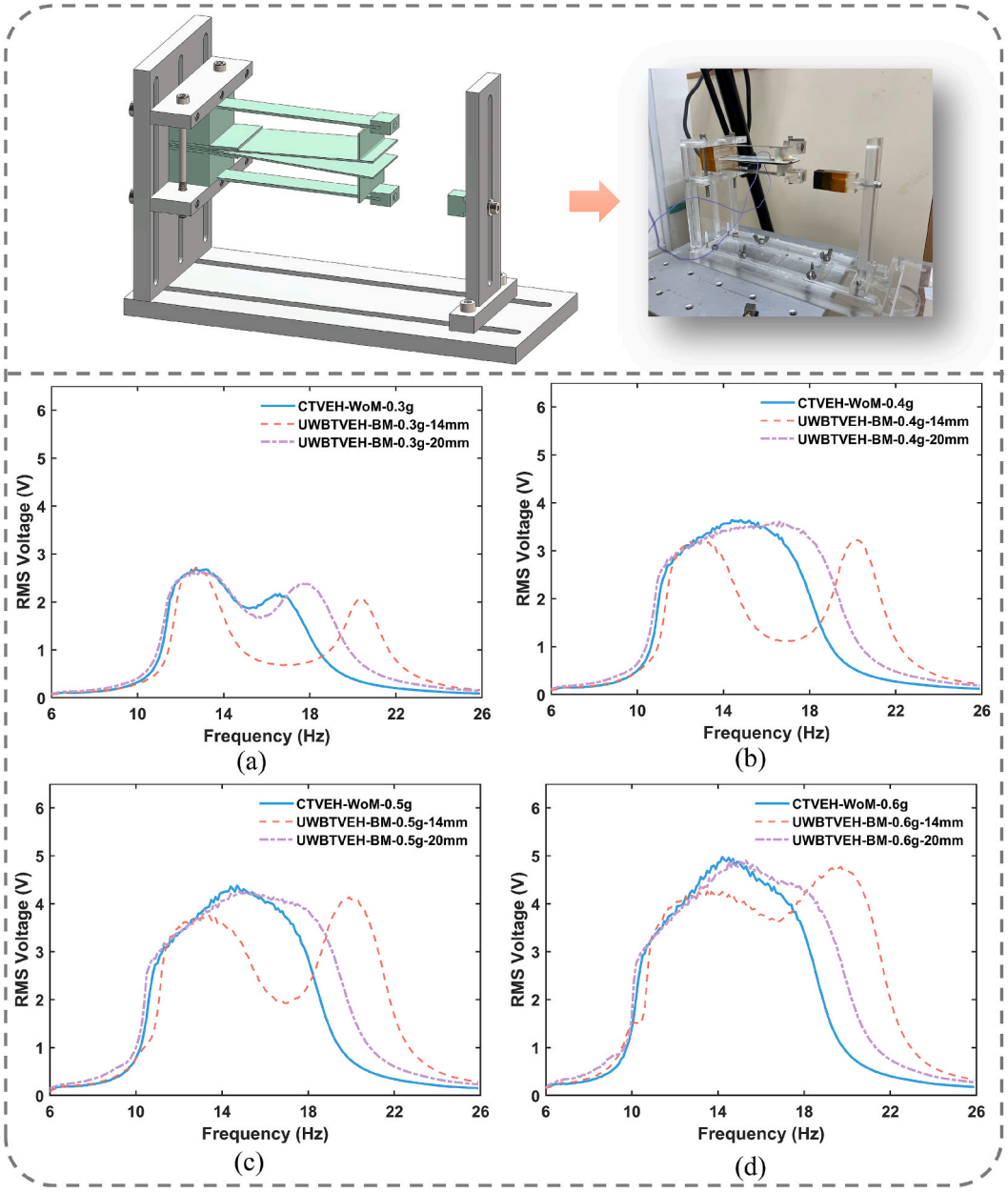

Fig. 8. UWBTVEH with only bottom magnet pair and RMS voltage output of UWBTVEH equipped with only bottom magnet pair with various gap distances and base accelerations: (a) 0.3 g; (b) 0.4 g; (c) 0.5 g and (d) 0.6 g.

frequencies, especially when the gap between the magnets is narrow, as seen in UWBTVEH-TM-0.3 g-14 mm and UWBTVEH-TM-0.4 g-14 mm. Generally, a smaller gap results in a stronger repulsive magnetic force, leading to more pronounced softening behavior in the beam. However, with a gap distance of 20 mm between the magnets, only one peak is observed under both low and high excitations, as shown in UWBTVEH-TM-0.3 g-20 mm and UWBTVEH-TM-0.6 g-20 mm (Fig. 7(a) and (d)). This suggests that the magnetic force is insufficient to overcome the strong coupling between the two beams. The voltage output of the UWBTVEH in the low-frequency range

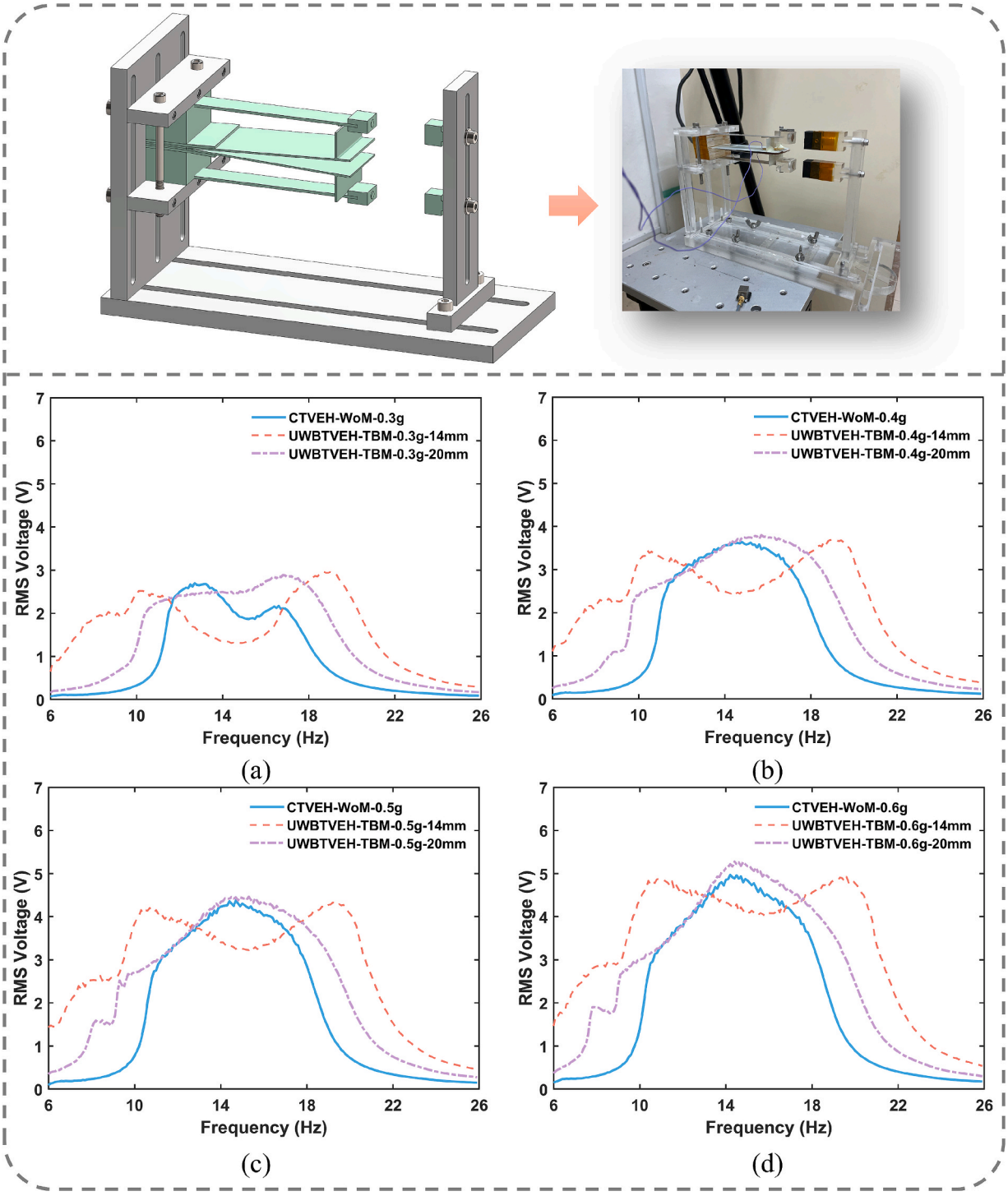

Fig. 9. UWBTVEH with both top and bottom magnet pairs and RMS voltage output of UWBTVEH equipped with top and bottom magnet pairs with various gap distances and base accelerations: (a) 0.3 g; (b) 0.4 g; (c) 0.5 g and (d) 0.6 g.

(6 Hz to 11 Hz) is higher than that of the CTVEH, suggesting that the rightward shift of the resonant frequency enhances the output in this lower frequency range. For configurations with a narrow gap and high excitation, such as UWBTVEH-TM-0.5 g-14 mm and UWBTVEH-TM-0.6 g-14 mm, the peaks become less distinct, and the harvester provides a more consistent output with a similar magnitude across a wider frequency range (Fig. 7(c) and (d)). This characteristic is advantageous for achieving continuous and wideband energy harvesting, making the UWBTVEH more effective under varying operational conditions.

6.2. UWBTVEH with only bottom magnet

The UWBTVEH with only a bottom magnet pair was also tested, as shown in Fig. 8. Under low excitation, two distinct peaks were observed for both CTVEH and UWBTVEH. The bottom magnet pair is in attractive configuration, which results in a hardening effect on the beam, thereby increasing its resonant frequency. By adjusting the gap between the magnets, the magnetic force can be controlled, allowing for precise tuning of the frequency shift. For instance, the second resonance peak shifts from 16.6 Hz to 17.7 Hz and 20.4 Hz for UWBTVEH-BM-0.3 g-20 mm and UWBTVEH-BM-0.3 g-14 mm, respectively (Fig. 8(a)). A frequency locking phenomenon is also observed in the UWBTVEH-BM-20 mm configuration when the excitation level exceeds 0.4 g. This occurs because the magnetic force is not strong enough to overcome the coupling between two beams (Fig. 8(b), (c) and (d)). However, when the gap distance is reduced to 14 mm, two clear peaks can also be seen for UWBTVEH-BM across the tested accelerations. Comparing the UWBTVEH-TM-0.3 g-14 mm and UWBTVEH-BM-0.3 g-14 mm with the CTVEH-WoM-0.3 g. It is evident that the first resonance peak shifts leftward from 12.8 Hz to 9 Hz, while the second peak shifts rightward from 16.6 Hz to 20.5 Hz. Although the net frequency shift is similar in these two cases, it is important to note that frequency locking in the higher frequency range requires a larger excitation due to the strong dependence of beam coupling on displacement. Overall, the results demonstrate that the employment of magnet pair in an attractive configuration provides significant flexibility in tuning the second resonance peak to the right.

6.3. UWBTVEH with both top and bottom magnets

The test results discussed in the previous sections successfully validate the capability of magnets to manipulate resonance by introducing either repulsive or attractive forces. Fig. 9 shows the UWBTVEH with both top and bottom magnet pairs, where the top pair is arranged in a repulsive configuration, and the bottom pair is in an attractive configuration. Similar tests were carried out for the UWBTVEH-TBM. In general, the first resonance peak shifts to the left, while the second peak shifts to the right compared to the CTVEH. Taking the UWBTVEH-TBM-0.3 g-14 mm as an example, the first peak shifts from 12.8 Hz to 10.3 Hz and the second peak shifts from 16.6 Hz to 19 Hz (Fig. 9(a)). The net frequency shift in this configuration is slightly smaller than that observed in individual magnet pair configuration, such as UWBTVEH-TM-0.3 g-14 mm and UWBTVEH-BM-0.3 g-14 mm. This reduction is likely due to partial cancellation of the repulsive and attractive forces, as the distance between the top and bottom magnetic pairs is not sufficiently large. As a result, the net force applied to each beam is reduced, leading to a smaller overall frequency shift. For the UWBTVEH-TBM with a gap distance of 20 mm, a frequency locking phenomenon is observed across all tested base accelerations, resulting in a single resonance peak (Fig. 9(a)-(d)). However, when the gap distance decreases to 14 mm, two distinct peaks are still present. These findings are fully consistent with the design predictions, confirming the ability to manipulate system resonance through the strategic use of magnetic forces.

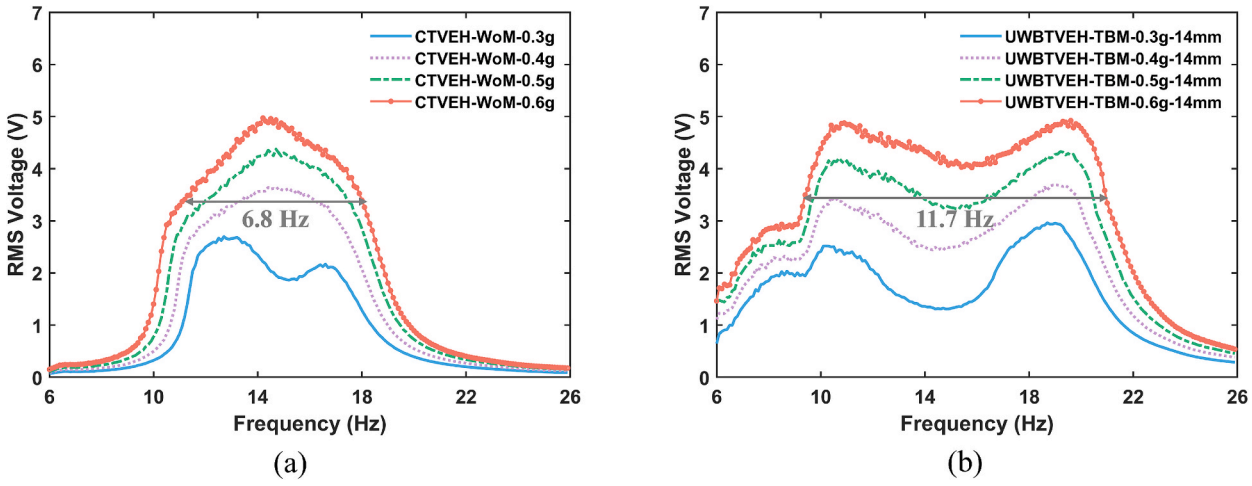

Fig. 10. The bandwidth comparison between CTVEH and UWBTVEH under various base accelerations.

6.4. Bandwidth analysis

The primary focus of this research is to design a wideband energy harvester by introducing nonlinear magnetic forces. Fig. 10 provides a direct comparison of the bandwidths between the CTVEH and UWBTVEH. In this context, bandwidth is evaluated based on the half-power definition, which is a standard method for assessing the operational frequency range of such devices. According to $P = V_{RMS}^2/R$, the half power is related to the $\sqrt{2}/2 \cdot V_{RMS}$ under the same external loading. Therefore, the bandwidth corresponds to the frequency range over which the V_{RMS} remains above 71 % of the peak value. For the CTVEH-WoM-0.6 g, the bandwidth is approximately 6.8 Hz. In contrast, the UWBTVEH-TBM-0.6 g-14 mm achieves a significantly wider bandwidth of 11.7 Hz, reflecting a remarkable 72 % improvement. This substantial increase demonstrates the effectiveness of incorporating both attractive and repulsive magnetic configurations to achieve bidirectional frequency tuning, thereby significantly enhancing the operational bandwidth of the energy harvester.

To evaluate the stability of the UWBTVEH, both upward and downward frequency sweeping tests were conducted. The results, shown in Fig. 11, demonstrate the harvester's excellent stability, as the voltage output remains almost consistent during bidirectional frequency sweeping. This behavior contrasts with traditional nonlinear energy harvesters, where the output from upward and downward frequency sweepings often fails to match perfectly, particularly near resonance, due to the jumping phenomenon. In summary, magnetic coupling is a dominant factor contributing to the wideband performance of the harvester. Other critical factors, such as the initial gap between the triboelectric layers and impact stiffness, also play essential roles in determining the bandwidth and have been discussed in detail in our previous studies. In such harvesters, it is challenging to achieve convergence to the high-energy orbit during downward frequency sweeping, leading to a lower output compared to the upward sweeping [49]. In the case of UWBTVEH, its performance is influenced not only by the nonlinearity of the individual beam components but also by the coupling effect between the two beams, resulting in a more stable dynamic response during bidirectional frequency sweeping. This enhanced stability is advantageous for energy harvesting from vibration sources with varying frequencies. Table 1 summarizes the wideband harvesters developed by other researchers. It is evident from the table that the UWBTVEH presents a novel approach in the design of wideband triboelectric energy harvester by utilizing nonlinear magnetic forces. While magnetic nonlinearity has been explored in the design of wideband piezoelectric energy harvesters (PEHs), it is worthwhile to note that a single PEH can only exhibit either hardening or softening behavior to broaden its bandwidth [50]. To achieve both hardening and softening behaviors simultaneously, two separate

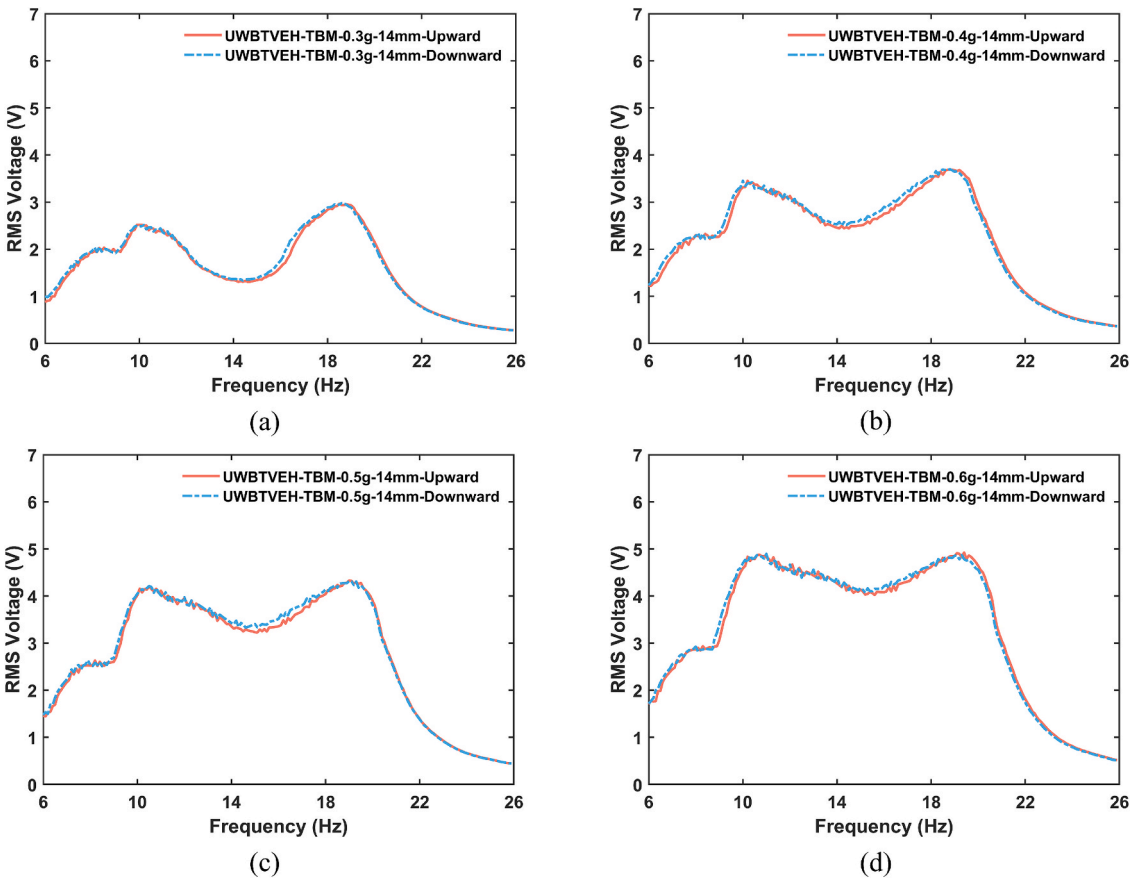

Fig. 11. RMS voltage output of UWBTVEH-TBM under various base accelerations during upward and downward frequency sweeping.

Table 1
Bandwidth comparison of UWBTVEH with other published triboelectric energy harvesters.

Wideband Techniques	Resonant Frequency (Hz)	Operating bandwidth (Hz)	Excitation Acceleration (g)	References
Bistability	5.5 Hz	4 Hz	–	[34]
Bistability	6 Hz	2 Hz	3.0 g	[35]
Impact nonlinearity	31.5 Hz	11.9 Hz	1.0 g	[27]
Impact nonlinearity	41 Hz	6 Hz	1.2 g	[53]
Impact nonlinearity	32 Hz	10 Hz	0.8 g	[24]
Tandem + Impact nonlinearity	20 Hz, 27 Hz, 34 Hz, 40 Hz	25 Hz	0.2 g	[54]
Multimodal + impact nonlinearity + magnetic nonlinearity	12.8 Hz, 16.6 Hz	11.7 Hz	0.6 g	This work

PEHs must be employed, necessitating additional circuit design due to the phase difference in output between the two PEHs [51,52]. In contrast, the unique working mechanism of the contact-separation mode in the TVEH allows a single unit to exhibit both hardening and softening behaviors without the need for complex circuitry. The distinct feature of the UWBTVEH offers a clear advantage over bistable triboelectric energy harvesters, which require much higher levels of acceleration compared to the proposed harvester, making them less suitable for energy harvesting in a low-acceleration environment [34,35]. Additionally, the UWBTVEH demonstrates superior stability compared to TVEHs that rely solely on impact nonlinearity, which often results in unmatched voltage output during bidirectional frequency sweeping. Notably, the UWBTVEH offers a competitive and continuous bandwidth compared to other existing harvesters, demonstrating its advantage for energy harvesting in low-frequency ranges and low-acceleration conditions [24,27,53]. Although Bhatia et al. reported a harvester with a bandwidth of 25 Hz under an excitation of 0.2 g, it should be noted that this wide bandwidth was achieved by utilizing four separate harvester units, each with a different resonant frequency. The average bandwidth for each harvester unit was around 7 Hz [54].

6.5. *Model validation*

The ultra-wideband property of the proposed UWBTVEH is highly dependent on the nonlinear magnetic force acting on the host beams. Thus, the accurate prediction of the magnetic force is very essential for validating the established electro-mechanical model. As discussed in Section 3.1, the MDM method is utilized to analyze the magnetic force between to magnets. To validate the accuracy of the calculated force, finite element method (FEM) is used to simulate the magnetic interaction between magnets as indicated in below Fig. 12. All the magnets are identical in dimension and magnetic flux density, with magnets *a* and *c* arranged in repulsive configuration, and magnets *b* and *d* in an attractive configuration. In the simulation, magnets *b*, *c* and *d* are fixed, while magnet *a* is allowed to move in the vertical direction. The magnet force applied on magnet *a* is calculated during is movement. Three different gap distances (d_h = 4 mm, 8 mm and 14 mm) were selected for the simulation. Fig. 13 compares the magnetic forces obtained from the FEM simulations with those obtained from the theoretical MDM model, showing good agreement, especially at larger gap distance. At smaller gap distance, such as $d_h = 4$ mm, the theoretical results exhibit some discrepancies compared to FEM results when magnet *a* is positioned further away from the paired magnet *c*. This deviation arises because the dipole approximation assumes that each magnet's field is primarily dipolar and that the distance between them is much larger than their characteristic dimensions. At close distance, higher-order multipole moments (e.g., quadrupoles, octupoles, etc.) start to play a significant role in the magnetic interaction, whereas, the MDM only considers the leading dipole term and ignores these higher-order terms, leading to inaccuracies at short distances [55]. It is worth noting that an extremely narrow gap distance is not recommended in harvester design as it usually requires

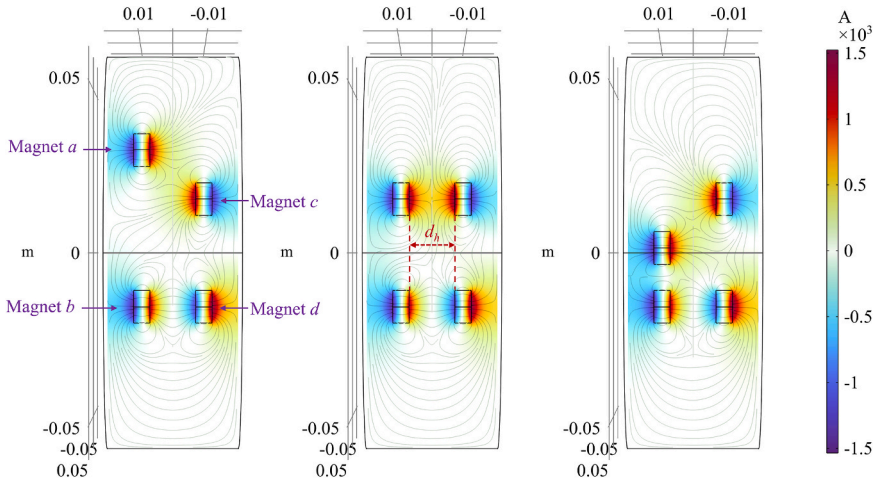

Fig. 12. Variation of the magnetic flux density with the movement of the magnet *a* when magnets *b*, *c* and *d* are fixed.

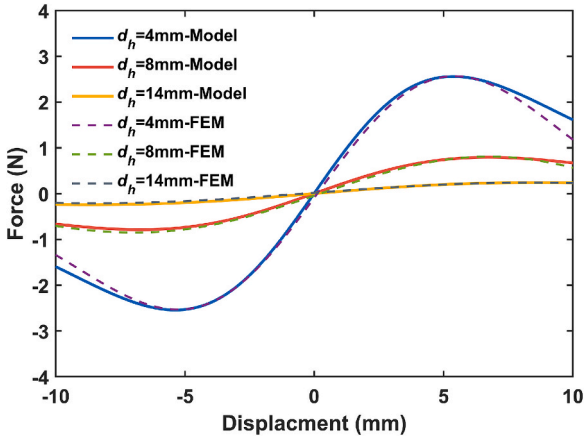

Fig. 13. Magnetic force of magnet a with varying gap distances between the paired magnets.

large excitation to overcome the high potential. In this this study, a relatively larger gap distance ($d_h = 14$ mm) is selected. Overall, the MDM provides high accuracy in calculating magnetic forces at larger gap distances, supporting its application in the design and analysis of the UWBTVEH.

The coupled electro-mechanical model is validated using the UWBTVEH-TBM-0.3 g-14 mm UWBTVEH-TBM-0.6 g-14 mm. Detailed mechanical, electrical and magnetic parameters of UWBTVEH are listed in below Table 2. The impact stiffness (k_c) and damping coefficient (c_c) are determined by trial and error to ensure alignment between simulated and experimental resonance. Both impact stiffness and damping coefficient are associated with the excitation level. In general, a higher excitation attributes to larger impact stiffness and damping [56]. In this study, $k_c = 500$ and 1000, and $c_c = 10$ and 18, are selected for excitations of 0.3 g and 0.6 g, respectively. These values are determined through trial and error to match the simulated resonance peaks with the experimental results for the CTVEH. Furthermore, it is worthwhile to mention that the beam exhibits a high intrinsic damping ratio due to the presence of joint elastomers, which are highly flexible and effectively absorb vibration energy. Additionally, friction between the contact pairs further contributes to an increase in system damping [57,58]. Fig. 14(a) shows the RMS voltage output from the harvester in the frequency domain. Good agreement between the experimental and analytical results can be observed for the UWBTVEH under both low and high excitations, which validates the accuracy of the established electro-mechanical model. In general, the displacement response of the harvester gradually increases during the upward frequency sweeping until reaching the peak at resonance. The enhanced displacement eases the contact between two triboelectric layers, resulting in a higher voltage output. However, a slight voltage drop occurs within a specific frequency range before the first resonance peak as highlighted by the dashed box in Fig. 14(a). Fig. 14(b) shows the voltage signal in time domain for UWBTVEH-TBM-0.3 g-14 mm at an excitation frequency of 9.2 Hz, displaying asymmetric voltage peaks. Specifically, the negative peaks have an irregular shape due to impact between the contacting layers, which further affects the RMS voltage output. Similar asymmetric and irregular voltage signals are observed in the simulated results as indicated in Fig. 14(c), further validating the accuracy of the established electro-mechanical model. In summary, the proposed model is

Table 2
Fundamental parameters used in the model validation.

Parameters	**Values**
Beam dimensions, Top & Bottom	$110 \times 15 \times 0.8$ mm^3
Mass density of beam, Top & Bottom	2700 kg/m^3
Young's modulus of beam, Top & Bottom	69 GPa
Tip mass, M_{t1} & M_{t2}	18.2 g; 9.3 g
Damping ratio, ζ_1 & ζ_2	0.2; 0.08
Location of motion transmission support, x_1	90 mm
PTFE film dimensions	$100 \times 40 \times 0.1$ mm^3
Copper film dimensions	$100 \times 40 \times 0.25$ mm^3
Aluminum foil dimensions	$100 \times 40 \times 0.1$ mm^3
Vacuum permittivity, ε_0	8.854×10^{-12}F/m
Relative permittivity of PTFE, ε_r	2.1
Thickness of PTFE, d	0.1 mm
External resistance, R	1 MΩ
Equivalent coefficient, ϑ	0.113
Surface charge density, σ	1.4×10^{-5}C/m^2
Magnet Radius, R_0	5 mm
Magnet length, $2T$	5 mm
Residual magnetic flux density, $\boldsymbol{Br}$	1.21
permeability of the vacuum, μ_0	$4\pi \times 10^{-7}$

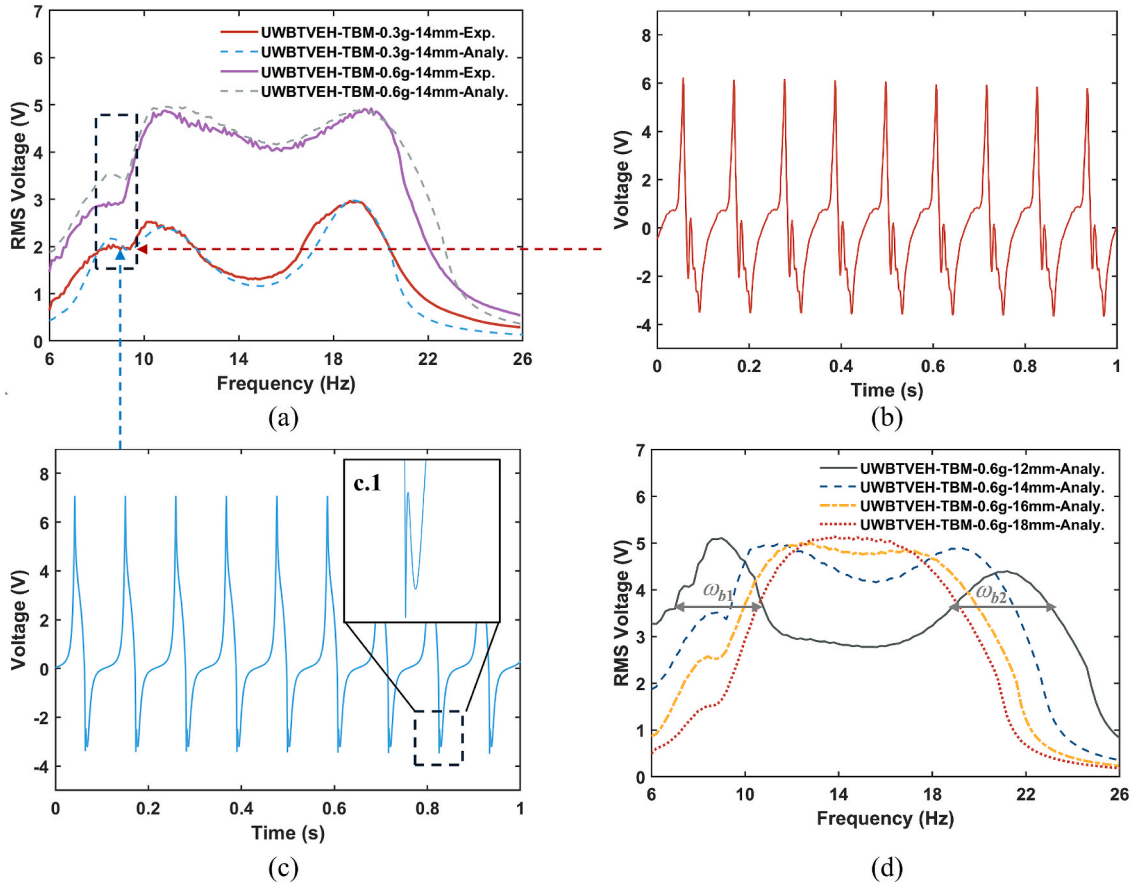

Fig. 14. Model validation of the proposed UWBTVEH: (a) comparison between the experimental and analytical results for UWBTVEH-TBM-0.3 g-14 mm and UWBTVEH-TBM-0.6 g-14 mm; (b) experimental voltage output in time domain for UWBTVEH-TBM-0.3 g-14 mm under an excitation frequency of 9.2 Hz; (c) simulated voltage output in time domain for UWBTVEH-TBM-0.3 g-14 mm under an excitation frequency of 9.2 Hz; (d) simulated RMS voltage output of UWBTVEH under various magnet gap distances ranging from 12 mm to 18 mm.

capable of capturing the major features of the harvester, including its wideband characteristics, RMS voltage magnitude and asymmetric voltage signals. This model provides valuable guidance for the design of wideband triboelectric energy harvesters.

To determine the optimal magnet distance for maximizing bandwidth in the current design, simulations were performed by varying only the magnet distance while keeping other parameters, such as magnet configuration and base excitation, unchanged. As illustrated in Fig. 14(d), the continuous bandwidth narrows as the magnet distance increases beyond 14 mm due to the diminished effect of magnetic force in achieving bidirectional frequency tuning. At a distance of 18 mm, the two resonant peaks tend to merge due to strong coupling between the two cantilever beams and the weaker influence of magnetic force. In general, a shorter magnet distance results in a stronger magnetic force. For instance, at a distance of 12 mm, two distinct peaks are observed, leading to discontinuous bandwidth (ω_{b1} and ω_{b2}) since the peaks are farther apart. The overall bandwidth in this case is smaller than that of the harvester with a 14 mm magnet distance. Further reducing the magnet distance induces bistability into the system, making it difficult for the system to overcome the potential barrier and significantly degrading power generation performance. Therefore, an optimal magnet distance (14 mm) exists in terms of maximizing the overall bandwidth, which is highly dependent on the nonlinear magnetic force introduced by the magnetic configuration. Additionally, other parameters, such as the system's initial resonances and the initial gap distance between the triboelectric layers, also play a critical role in determining the performance.

7. Performance characterization

The ultimate goal of small-scale energy harvesting is to enable self-powered IoT sensing. To evaluate the advantages of a wideband energy harvester, the UWBTVEH-TBM-0.6 g-14 mm was selected to power a sensing module equipped with an integrated energy management unit (EMU) and a temperature sensor [2]. The experimental setup is shown in Fig. 15(a). The output from the UWBTVEH is directed to the EMU to charge a capacitor, with a multimeter placed nearby to measure the capacitor's voltage. Once the capacitor voltage reaches 5 V, a signal transmission is triggered and sent to the mobile device via Bluetooth, allowing the sensor location and monitored temperature to be viewed on the phone as indicated in Fig. 15(b). Fig. 15(c) displays the charging curve for two capacitors

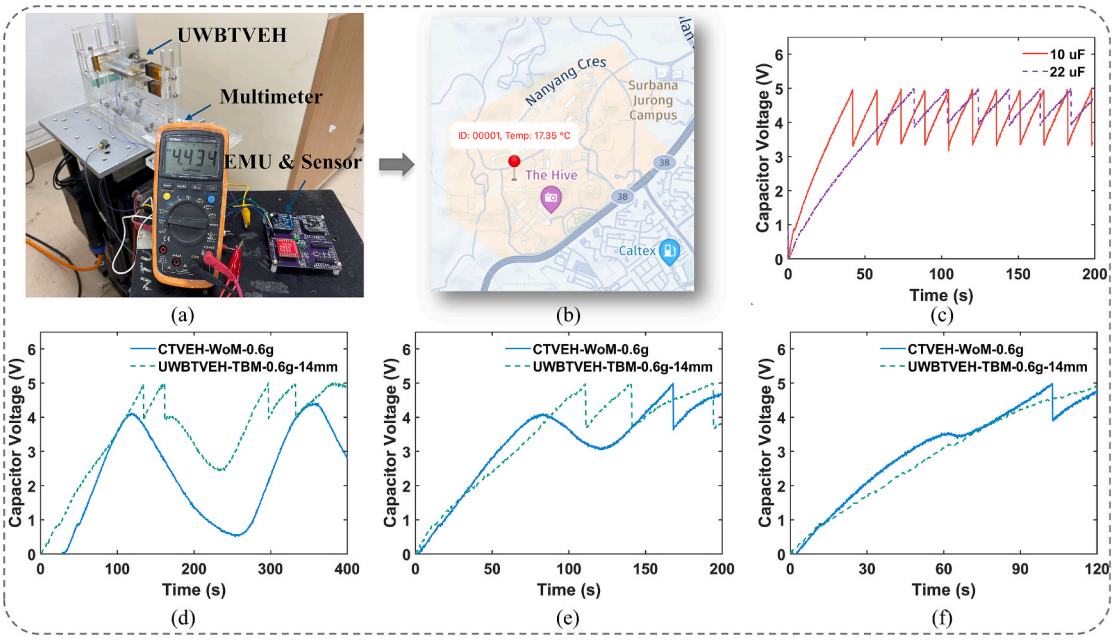

Fig. 15. (a) Demonstration setup for the UWBTVEH; (b) display interface of the IoT system; (c) charging curves for the capacitor with different capacitances; IoT demonstration of UWBTVEH and CTVEH under different frequency sweeping ranges: (d) 6 Hz-26 Hz; (e) 10 Hz-20 Hz and (f) 12 Hz-18 Hz.

with capacitances of 10 μF and 22 μF. It can be observed that the clod start time (0 V – 5 V) for the 10 μF capacitor is much shorter than that for the 22 μF capacitor. Within the same charging period of 80 s, the 10 μF capacitor enabled 11 signal transmissions, whereas the 22 μF capacitor allowed for only 6 transmissions. These results effectively demonstrate the ability of the UWBTVEH in self-powered IoT sensing. The advantage of a wideband energy harvester lies in its ability to generate power effectively under varying frequencies. To validate the performance of the UWBTVEH, the UWBTVEH-TBM-0.6 g-14 mm was used to power a sensing module during frequency sweeping, with the CTVEH-WoM-0.6 g also tested for comparison. Three different sweeping ranges were considered and the sweeping rate was controlled at 0.1 Hz/s. The test also considered the upward and downward sweeping processes. Fig. 15(d) shows that the CTVEH could only charge the capacitor to around 4 V within the 6 Hz to 26 Hz range and was unable to trigger the signal transmission. In contrast, the UWBTVEH achieved 4 signal transmissions within the same time, indicating that the UWBTVEH generated more energy from the vibration source. In Fig. 15(e), the CTVEH managed to transmit one signal within the 10 Hz to 20 Hz range, while the UWBTVEH transmitted three signals in the same period. When the frequency sweeping range was narrowed to 12 Hz to 18 Hz, as shown in Fig. 15(f). the CTVEH was able to transmit one signal, while the UWBTVEH could not trigger the sensing module's operation. This outcome is attributed to the higher output of the CTVEH with that narrow range, as indicated in Fig. 10(a). It can be concluded that the UWBTVEH outperforms the CTVEH when the vibration source exhibits a wider frequency variation ($>$ 6 Hz). Therefore, selecting between CTVEH and UWBTVEH involves a trade-off that depends on the variability of the vibration source. For concentrated and stable vibrations, the CTVEH is a suitable choice. Conversely, for unstable and variable ambient vibrations, the UWBTVEH is preferable.

8. Conclusions

This study presents a novel approach for designing triboelectric energy harvesters by integrating magnetic configurations. By strategically employing attractive and repulsive magnetic forces on structures connected to triboelectric layers, the design achieves wideband energy harvesting capability. The proposed concept was validated through a compact, cost-effective cantilever-type harvester, UWBTVEH, specifically designed to capture low-frequency and low-acceleration ambient vibrations. Comprehensive experimental and theoretical analyses were conducted to assess the design methodology and evaluate the performance of the UWBTVEH. The key conclusions of this work are drawn as follows:

- This study proposes a unique method for achieving wideband performance in triboelectric energy harvesters by incorporating magnetic configurations. Unlike conventional bandwidth-broadening methods such as impact nonlinearity and multimodal techniques, the proposed method utilizes nonlinear magnetic forces to bidirectionally tune the resonances of cantilever beams, significantly expanding the operational bandwidth.
- A series of experimental tests were conducted on the fabricated UWBTVEH prototype, examining three distinct magnetic configurations: (1) repulsive configuration (top magnetic pair only), (2) attractive configuration (bottom magnetic pair only), and (3)

combined repulsive and attractive configuration (top and bottom magnetic pairs). The results clearly demonstrate the ability of magnetic interactions to tune the bandwidth. Specifically, for the optimal configuration (UWBTVEH-TBM-0.6 g-14 mm), a total bandwidth of 11.7 Hz was achieved, representing a 71 % increase in bandwidth compared to the harvester without magnetic interactions.

- An electro-mechanical model incorporating the impact forces between triboelectric layers, external magnetic forces, and the non-parallel configuration of triboelectric layers was developed. The model was experimentally validated, accurately predicting the UWBTVEH's wideband behavior and voltage output, underscoring its utility for design optimization.
- The power generation capability of the UWBTVEH was assessed using an IoT platform. The harvester successfully charges a 10 μF capacitor to 5 V within 18 s, enabling wireless signal transmission for a sensing module. The harvester demonstrated superior performance compared to conventional harvesters across varying excitation frequencies, highlighting its potential for self-powered IoT systems.

This study underscores the versatility of the proposed magnetic configuration methodology, which can be extended to various host structures connected to triboelectric layers. Furthermore, it emphasizes the importance of considering nonlinear dynamic behavior of triboelectric layers in harvester design, as its performance relies on the coupled interactions between these layers. These findings provide valuable guidance for the development of next-generation triboelectric energy harvesters tailored for wideband energy harvesting in real-world applications.

CRediT authorship contribution statement

Chaoyang Zhao: Writing – original draft, Methodology, Conceptualization. **Xin Li:** Validation, Resources. **Liwei Dong:** Visualization, Investigation. **Guobiao Hu:** Software, Resources, Investigation. **Chengjia Han:** Validation, Formal analysis. **Yiqing Dong:** Validation, Formal analysis. **Liya Zhao:** Writing – review & editing, Investigation. **Yaowen Yang:** Writing – review & editing, Supervision.

Declaration of competing interest

The authors declare that they have no known competing financial interests or personal relationships that could have appeared to influence the work reported in this paper.

Data availability

Data will be made available on request.

References

[1] Q. Zhang, C. Xin, F. Shen, Y. Gong, Y. Zi, H. Guo, Z. Li, Y. Peng, Q. Zhang, Z.L. Wang, *Human body IoT systems based on the triboelectrification effect: energy harvesting, sensing, interfacing and communication*, *Energy Environ. Sci.* 15 (2022) 3688–3721, https://doi.org/10.1039/D2EE01590K.
[2] X. Li, L. Teng, H. Tang, J. Chen, H. Wang, Y. Liu, M. Fu, J. Liang, *ViPSN: A Vibration-Powered IoT Platform*, *IEEE Internet Things J.* 8 (2021) 1728–1739, https://doi.org/10.1109/jiot.2020.3016993.
[3] *Q. Zheng, L. Xin, Q. Zhang, F. Shen, X. Lu, C. Cao, C. Xin, Y. Zhao, H. Liu, Y. Peng, J. Luo, H. Guo, Z. Li, Leech-Inspired Amphibious Soft Robot Driven by High-Voltage Triboelectricity, Advanced Materials n/a (n.d.) 2417380. https://doi.org/10.1002/adma.202417380.*
[4] X. Su, Y. Leng, S. Sun, X. Chen, J. Xu, *Theoretical and experimental investigation of a quad-stable piezoelectric energy harvester using a locally demagnetized multi-pole magnet*, *Energ. Conver. Manage.* 271 (2022) 116291, https://doi.org/10.1016/j.enconman.2022.116291.
[5] R.M. Toyabur, M. Salauddin, H. Cho, J.Y. Park, *A multimodal hybrid energy harvester based on piezoelectric-electromagnetic mechanisms for low-frequency ambient vibrations*, *Energ. Conver. Manage.* 168 (2018) 454–466, https://doi.org/10.1016/j.enconman.2018.05.018.
[6] S.X. Zhou, J.Y. Cao, D.J. Inman, J. Lin, S.S. Liu, Z.Z. Wang, *Broadband tristable energy harvester: Modeling and experiment verification*, *Appl. Energy* 133 (2014) 33–39, https://doi.org/10.1016/j.apenergy.2014.07.077.
[7] H. Fu, E.M. Yeatman, *Effective piezoelectric energy harvesting using beam plucking and a synchronized switch harvesting circuit*, *Smart Mater. Struct.* 27 (2018), https://doi.org/10.1088/1361-665X/aac0ba.
[8] S.X. Zhou, J.Y. Cao, A. Erturk, J. Lin, *Enhanced broadband piezoelectric energy harvesting using rotatable magnets*, *Appl. Phys. Lett.* 102 (2013), https://doi.org/10.1063/1.4803445.
[9] S. Ji, X. Liao, *Researches on MEMS thermoelectric-photoelectric integrated energy harvester with metal heat sink*, *Microelectron. J.* 96 (2020) 104702, https://doi.org/10.1016/j.mejo.2020.104702.
[10] Y. Jia, P. Liu, L. Bao, J. Sui, J. Zhao, J. Wang, *Transduction of UV-light energy into alternating-current electricity via a neglected internal photoelectric effect of metal foil-based nanogenerator*, *Nano Energy* 120 (2024) 109174, https://doi.org/10.1016/j.nanoen.2023.109174.
[11] *Science Advance* (2018).
[12] M.A. Alghoul, S.A. Shahahmadi, B. Yeganeh, N. Asim, A.M. Elbreki, K. Sopian, S.K. Tiong, N. Amin, *A review of thermoelectric power generation systems: Roles of existing test rigs/ prototypes and their associated cooling units on output performance*, *Energ. Conver. Manage.* 174 (2018) 138–156, https://doi.org/10.1016/j.enconman.2018.08.019.
[13] H. Zhang, L.J. Yao, L.W. Quan, X.L. Zheng, *Theories for triboelectric nanogenerators: A comprehensive review*, *Nanotechnol. Rev.* 9 (2020) 610–625, https://doi.org/10.1515/ntrev-2020-0049.
[14] Y.L. Zi, L. Lin, J. Wang, S.H. Wang, J. Chen, X. Fan, P.K. Yang, F. Yi, Z.L. Wang, *Triboelectric-Pyroelectric-Piezoelectric Hybrid Cell for High-Efficiency Energy-Harvesting and Self-Powered Sensing*, *Adv. Mater.* 27 (2015) 2340–2347, https://doi.org/10.1002/adma.201500121.
[15] Y. Wang, H. Du, H. Yang, Z. Xi, C. Zhao, Z. Qian, X. Chuai, X. Peng, H. Yu, Y. Zhang, X. Li, G. Hu, H. Wang, M. Xu, *A rolling-mode triboelectric nanogenerator with multi-tunnel grating electrodes and opposite-charge-enhancement for wave energy harvesting*, *Nat Commun* 15 (2024) 1–11, https://doi.org/10.1038/s41467-024-51245-5.

[16] C. Wu, R. Liu, J. Wang, Y. Zi, L. Lin, Z.L. Wang, *A spring-based resonance coupling for hugely enhancing the performance of triboelectric nanogenerators for harvesting low-frequency vibration energy*, *Nano Energy* 32 (2017) 287–293, https://doi.org/10.1016/j.nanoen.2016.12.061.

[17] S. Li, D. Liu, Z. Zhao, L. Zhou, X. Yin, X. Li, Y. Gao, C. Zhang, Q. Zhang, J. Wang, Z.L. Wang, *A Fully Self-Powered Vibration Monitoring System Driven by Dual-Mode Triboelectric Nanogenerators*, *ACS Nano* 14 (2020) 2475–2482, https://doi.org/10.1021/acsnano.9b10142.

[18] Y. Chen, Y.-C. Wang, Y. Zhang, H. Zou, Z. Lin, G. Zhang, C. Zou, Z.L. Wang, *Elastic-Beam Triboelectric Nanogenerator for High-Performance Multifunctional Applications: Sensitive Scale, Acceleration/Force/Vibration Sensor, and Intelligent Keyboard*, *Adv. Energy Mater.* 8 (2018), https://doi.org/10.1002/aenm.201802159.

[19] G. Hu, C. Zhao, Y. Yang, X. Li, J. Liang, *Triboelectric energy harvesting using an origami-inspired structure*, *Appl. Energy* 306 (2022), https://doi.org/10.1016/j.apenergy.2021.118037.

[20] J. He, X. Fan, J. Mu, C. Wang, J. Qian, X. Li, X. Hou, W. Geng, X. Wang, X. Chou, *3D full-space triboelectric-electromagnetic hybrid nanogenerator for high-efficient mechanical energy harvesting in vibration system*, *Energy* 194 (2020) 116871, https://doi.org/10.1016/j.energy.2019.116871.

[21] L.-Q. Chen, Y. Fan, *Internal resonance vibration-based energy harvesting*, *Nonlinear Dyn* 111 (2023) 11703–11727, https://doi.org/10.1007/s11071-023-08464-0.

[22] X. Wang, C. Chen, N. Wang, H. San, Y. Yu, E. Halvorsen, X. Chen, *A frequency and bandwidth tunable piezoelectric vibration energy harvester using multiple nonlinear techniques*, *Appl. Energy* 190 (2017) 368–375, https://doi.org/10.1016/j.apenergy.2016.12.168.

[23] Y. Fu, H. Ouyang, R.B. Davis, *Triboelectric energy harvesting from the vibro-impact of three cantilevered beams*, *Mech. Syst. Sig. Process.* 121 (2019) 509–531, https://doi.org/10.1016/j.ymssp.2018.11.043.

[24] A. Ibrahim, A. Ramini, S. Towfighian, *Experimental and theoretical investigation of an impact vibration harvester with triboelectric transduction*, *J. Sound Vib.* 416 (2018) 111–124, https://doi.org/10.1016/j.jsv.2017.11.036.

[25] Z. Yang, N. Ismail, C. Son, P.M. Ferreira, S. Kim, *Broadband, Tunable, Miniaturized Vibration Energy Harvester Using Nonlinear Elastomer Beams and Stretchable Interconnects*, *Adv. Mater. Technol.* 4 (2019), https://doi.org/10.1002/admt.201900783.

[26] R.K. Gupta, Q.F. Shi, L. Dhakar, T. Wang, C.H. Heng, C. Lee, *Broadband Energy Harvester Using Non-linear Polymer Spring and Electromagnetic/Triboelectric Hybrid Mechanism*, *Sci. Rep.* 7 (2017), https://doi.org/10.1038/srep41396.

[27] L. Dhakar, F.E.H. Tay, C.K. Lee, *Investigation of contact electrification based broadband energy harvesting mechanism using elastic PDMS microstructures*, *J. Micromech. Microeng.* 24 (2014), https://doi.org/10.1088/0960-1317/24/10/104002.

[28] J. Yang, J. Chen, Y. Yang, H. Zhang, W. Yang, P. Bai, Y. Su, Z.L. Wang, *Broadband Vibrational Energy Harvesting Based on a Triboelectric Nanogenerator*, *Adv. Energy Mater.* 4 (2014), https://doi.org/10.1002/aenm.201301322.

[29] G. Tang, F. Cheng, X. Hu, B. Huang, B. Xu, Z. Li, X. Yan, D. Yuan, W. Wu, Q. Shi, *A Two-Degree-of-Freedom Cantilever-Based Vibration Triboelectric Nanogenerator for Low-Frequency and Broadband Operation*, *Electronics* 8 (2019) 1526, https://doi.org/10.3390/electronics8121526.

[30] G. Xu, C. Li, C. Chen, J. Fu, T. Hou, Y. Zi, *Dynamics of triboelectric nanogenerators: A review*, *Int Journal of Mech Sys Dyn* 2 (2022) 311–324, https://doi.org/10.1002/msd2.12058.

[31] L. Zhao, Y. Gong, F. Shen, Y. Peng, S. Xie, Z. Li, *Diminishing potential well barrier in bi-stable energy harvesters by introducing symmetric stiffness*, *Thin-Walled Struct.* 209 (2025) 112880, https://doi.org/10.1016/j.tws.2024.112880.

[32] L. Zhao, G. Hu, S. Zhou, Y. Peng, S. Xie, Z. Li, *Magnetic coupling and amplitude truncation based bistable energy harvester*, *Int. J. Mech. Sci.* 273 (2024) 109228, https://doi.org/10.1016/j.ijmecsci.2024.109228.

[33] T. Liu, C. Zhao, Y. Yang, W. Yuan, *Nonlinear vibration of a loaded string in energy harvesting*, *Smart Mater. Struct.* 33 (2024) 105027, https://doi.org/10.1088/1361-665X/ad79cf.

[34] D. Tan, J. Zhou, K. Wang, X. Zhao, Q. Wang, D. Xu, *Bow-type bistable triboelectric nanogenerator for harvesting energy from low-frequency vibration*, *Nano Energy* 92 (2022) 106746, https://doi.org/10.1016/j.nanoen.2021.106746.

[35] H. Luo, J. Liu, T. Yang, Y. Zhang, Q. Cao, *Dipteran flight-inspired bistable triboelectric nanogenerator for harvesting low frequency vibration*, *Nano Energy* 103 (2022) 107755, https://doi.org/10.1016/j.nanoen.2022.107755.

[36] Z.L. Wang, J. Chen, L. Lin, *Progress in triboelectric nanogenerators as a new energy technology and self-powered sensors*, *Energy Environ. Sci.* 8 (2015) 2250–2282, https://doi.org/10.1039/c5ee01532d.

[37] L. Tang, Y. Yang, *A nonlinear piezoelectric energy harvester with magnetic oscillator*, *Appl. Phys. Lett.* 101 (2012), https://doi.org/10.1063/1.4748794.

[38] D. Upadrashta, Y. Yang, *Finite element modeling of nonlinear piezoelectric energy harvesters with magnetic interaction*, *Smart Mater. Struct.* 24 (2015), https://doi.org/10.1088/0964-1726/24/4/045042.

[39] L. Tian, H. Shen, Q. Yang, R. Song, Y. Bian, *A novel outer-inner magnetic two degree-of-freedom piezoelectric energy harvester*, *Energ. Conver. Manage.* 283 (2023) 116920, https://doi.org/10.1016/j.enconman.2023.116920.

[40] A. Erturk, D.J. Inman, *On Mechanical Modeling of Cantilevered Piezoelectric Vibration Energy Harvesters*, *J. Intell. Mater. Syst. Struct.* 19 (2008) 1311–1325, https://doi.org/10.1177/1045389x07085639.

[41] G.B. Hu, J.L. Wang, L.H. Tang, *A comb-like beam based piezoelectric system for galloping energy harvesting*, *Mech. Syst. Sig. Process.* 150 (2021), https://doi.org/10.1016/j.ymssp.2020.107301.

[42] H.T. Li, W.Y. Qin, J. Zu, Z. Yang, *Modeling and experimental validation of a buckled compressive-mode piezoelectric energy harvester*, *Nonlinear Dyn* 92 (2018) 1761–1780, https://doi.org/10.1007/s11071-018-4160-y.

[43] D. Tan, Y.G. Leng, Y.J. Gao, *Magnetic force of piezoelectric cantilever energy harvesters with external magnetic field*, *Eur. Phys. J. Spec. Top.* 224 (2015) 2839–2853, https://doi.org/10.1140/epjst/e2015-02592-6.

[44] G. Akoun, J.-P. Yonnet, *3D analytical calculation of the forces exerted between two cuboidal magnets*, *IEEE Trans. Magn.* 20 (1984) 1962–1964, https://doi.org/10.1109/TMAG.1984.1063554.

[45] Y. Yang, H. Xiang, *A simple and precise formula for magnetic forces in nonlinear piezoelectric energy harvesting*, *Nonlinear Dyn* 111 (2023) 6085–6110, https://doi.org/10.1007/s11071-022-08160-5.

[46] C. Zhao, G. Hu, Y. Yang, *A cantilever-type vibro-impact triboelectric energy harvester for wind energy harvesting*, *Mech. Syst. Sig. Process.* 177 (2022), https://doi.org/10.1016/j.ymssp.2022.109185.

[47] C.Y. Zhao, Y.W. Yang, D. Upadrashta, L.Y. Zhao, *Design, modeling and experimental validation of a low-frequency cantilever triboelectric energy harvester*, *Energy* 214 (2021), https://doi.org/10.1016/j.energy.2020.118885.

[48] C. Zhao, G. Hu, X. Li, Z. Liu, W. Yuan, Y. Yang, *Wide-bandwidth triboelectric energy harvester combining impact nonlinearity and multi-resonance method*, *Appl. Energy* 348 (2023) 121530, https://doi.org/10.1016/j.apenergy.2023.121530.

[49] M.F. Daqaq, R. Masana, A. Erturk, D. Dane Quinn, *On the Role of Nonlinearities in Vibratory Energy Harvesting: A Critical Review and Discussion*, *Appl. Mech. Rev.* 66 (2014) 040801, https://doi.org/10.1115/1.4026278.

[50] O.V. Gendelman, *Analytic treatment of a system with a vibro-impact nonlinear energy sink*, *J. Sound Vib.* 331 (2012) 4599–4608, https://doi.org/10.1016/j.jsv.2012.05.021.

[51] Z.B. Yang, S.X. Zhou, J. Zu, D. Inman, *High-Performance Piezoelectric Energy Harvesters and Their Applications*, *Joule* 2 (2018) 642–697, https://doi.org/10.1016/j.joule.2018.03.011.

[52] I.C. Lien, Y.C. Shu, *Array of piezoelectric energy harvesting by the equivalent impedance approach*, *Smart Mater. Struct.* 21 (2012) 082001, https://doi.org/10.1088/0964-1726/21/8/082001.

[53] H. Abumarar, A. Ibrahim, *A Nonlinear Impact-Driven Triboelectric Vibration Energy Harvester for Frequency Up-Conversion*, *Micromachines* 14 (2023) 1082, https://doi.org/10.3390/mi14051082.

[54] D. Bhatia, W. Kim, S. Lee, S.W. Kim, D. Choi, *Tandem triboelectric nanogenerators for optimally scavenging mechanical energy with broadband vibration frequencies*, *Nano Energy* 33 (2017) 515–521, https://doi.org/10.1016/j.nanoen.2017.01.059.

[55] Y. Sui, K. Leslie, D. Clark, *Multiple-Order Magnetic Gradient Tensors for Localization of a Magnetic Dipole*, *IEEE Magn. Lett.* 8 (2017) 1–5, https://doi.org/10.1109/LMAG.2017.2708682.

[56] W. Sim, B. Lee, D.J. Kim, J.A. Lee, J. Kim, J. Chung, *Vibro-impact analysis of two adjacent cantilever beams*, *Nonlinear Dyn.* 108 (2022) 987–1004, https://doi.org/10.1007/s11071-022-07246-4.
[57] K. Popp, L. Panning, W. Sextro, *Vibration Damping by Friction Forces: Theory and Applications*, *J. Vib. Control* 9 (2003) 419–448, https://doi.org/10.1177/107754603030780.
[58] L. Gagnon, M. Morandini, G.L. Ghiringhelli, *A review of friction damping modeling and testing*, *Arch Appl Mech* 90 (2020) 107–126, https://doi.org/10.1007/s00419-019-01600-6.